

REPORT DOCUMENTATION PAGE				Form Approved OMB No. 0704-0188	
<small>The public reporting burden for this collection of information is estimated to average 1 hour per response, including the time for reviewing instructions, searching existing data sources, gathering and maintaining the data needed, and completing and reviewing the collection of information. Send comments regarding this burden estimate or any other aspect of this collection of information, including suggestions for reducing the burden, to Department of Defense, Washington Headquarters Services, Directorate for Information Operations and Reports (0704-0188), 1215 Jefferson Davis Highway, Suite 1204, Arlington, VA 22202-4302. Respondents should be aware that notwithstanding any other provision of law, no person shall be subject to any penalty for failing to comply with a collection of information if it does not display a currently valid OMB control number.</small> PLEASE DO NOT RETURN YOUR FORM TO THE ABOVE ADDRESS.					
1. REPORT DATE (DD-MM-YYYY) 12-05-2010		2. REPORT TYPE		3. DATES COVERED (From - To)	
4. TITLE AND SUBTITLE Strangeness Production in 19.6 GeV Collisions at the Relativistic Heavy Ion Collider			5a. CONTRACT NUMBER		
			5b. GRANT NUMBER		
			5c. PROGRAM ELEMENT NUMBER		
6. AUTHOR(S) Englund-Krieger, Kyle Richard			5d. PROJECT NUMBER		
			5e. TASK NUMBER		
			5f. WORK UNIT NUMBER		
7. PERFORMING ORGANIZATION NAME(S) AND ADDRESS(ES)			8. PERFORMING ORGANIZATION REPORT NUMBER		
9. SPONSORING/MONITORING AGENCY NAME(S) AND ADDRESS(ES) U.S. Naval Academy Annapolis, MD 21402			10. SPONSOR/MONITOR'S ACRONYM(S)		
			11. SPONSOR/MONITOR'S REPORT NUMBER(S) Trident Scholar Report no. 387 (2010)		
12. DISTRIBUTION/AVAILABILITY STATEMENT This document has been approved for public release; its distribution is UNLIMITED					
13. SUPPLEMENTARY NOTES					
14. ABSTRACT The goal of this research is to try to discover what occurred during the first three milliseconds of the universe. As of now, Quark-Gluon Plasma, QGP, is what scientists believe existed at the beginning. QGP is studied through the STAR Experiment at the Relativistic Heavy Ion Collider. Mass distributions and fitted transverse momentum spectrum for K <sup>0</sup> <sub>S</sub> , Λ, and anti-Λ's were developed. The ratio of Λ to anti-Λ's was found.					
15. SUBJECT TERMS Strangeness Production, Relativistic Heavy Ion Collider, STAR Experiment, Lamda Particles					
16. SECURITY CLASSIFICATION OF:			17. LIMITATION OF ABSTRACT	18. NUMBER OF PAGES 67	19a. NAME OF RESPONSIBLE PERSON
a. REPORT	b. ABSTRACT	c. THIS PAGE			19b. TELEPHONE NUMBER (Include area code)

U.S.N.A. --- Trident Scholar Project Report; no. 387 (2010)

**STRANGENESS PRODUCTION IN 19.6 GeV COLLISIONS AT THE RELATIVISTIC  
HEAVY ION COLLIDER**

By

Midshipman 1/c Kyle R. Englund-Krieger  
United States Naval Academy  
Annapolis, Maryland

---

Certification of Adviser Approval  
Assistant Professor Richard A. Witt  
Physics Department

---

Acceptance for the Trident Scholar Committee  
Professor Carl E. Wick  
Associate Director of Midshipman Research

---

“Science can purify religion from error and superstition;

Religion can purify science from idolatry and false absolutes.

Each can draw the other into a wider world, a world in which both can flourish ”

-Pope John Paul II

# Strangeness Production in 19.6 GeV Collisions at the Relativistic Heavy Ion Collider

List of Figures

List of Symbols and Acronyms

1. Background and Beginnings
  - 1.1. Understanding High Energy Particle Physics
    - 1.1.1. Particle Physics Background
    - 1.1.2. Nuclear Critical Point
    - 1.1.3. Heavy Ion Collisions
  - 1.2. Brookhaven National Labs and the Relativistic Heavy Ion Collider (RHIC)
    - 1.2.1. The Machine
    - 1.2.2. The Solenoidal Tracker at RHIC (STAR) and the Time Projection Chamber
    - 1.2.3. Geometry of Collisions
2. Initial Data Processing
  - 2.1. Raw Mass Distributions
  - 2.2. Event Level Cut
  - 2.3. Creation of Raw Mass Histograms
3. Analysis and Background Reduction
  - 3.1. Reducing the Background
    - 3.1.1. Rapidity Cut
    - 3.1.2. Decay Length of the V0
    - 3.1.3. Number of Detector Hits
    - 3.1.4. Distance of Closest Approach Cuts
    - 3.1.5. Cut on the NSigma
  - 3.2. Resultant  $K_S^0$ ,  $\Lambda$ , or anti- $\Lambda$  Histograms
    - 3.2.1. Mass Peaks
    - 3.2.2. Bin Counting and Sideband Subtraction
4. Transverse Momentum Spectrum
  - 4.1. Transverse Momentum Binning
  - 4.2. Transverse Momentum Spectrum
5. Corrections
6. Results
7. Conclusions and Outlook

Acknowledgements

## List of Figures

Figure 1.1: Nucleus Breakdown

Figure 1.2: Well known Baryons and Anti-Baryons

Figure 1.3: Well known Mesons

Figure 1.4: Phase Diagram of Nuclear Matter

Figure 1.5: The author and his advisor together with MIDN 3/C Hernandez and LCDR Ita beside the superconducting rings of RHIC

Figure 1.6: Beam Line view of a single Au-Au Collision in STAR

Figure 1.7: Ion Acceleration Process at Brookhaven

Figure 1.8: Cross-Section of the STAR Experiment

Figure 1.9: The STAR Detector

Figure 1.10: A Super Sector of the TPC

Figure 1.11: Side View of a Reconstructed Au+Au Collision

Figure 1.12: Description of Impact Parameter

Figure 1.13: Image of a non-central collision

Figure 2.1: Histogram of the Primary Vertex Position Cut at 50 cm

Figure 2.2: Beam line diagram of how events are reconstructed in the TPC

Figure 2.3: Raw Lambda Mass Distribution before any cuts are applied to the data

Figure 2.4: Raw Anti Lambda Mass Distribution before any cuts are applied

Figure 2.5: Raw Mass Distribution of  $K^0$ 's particles before any cuts are applied

Figure 3.1: Plot of Decay Length for the  $\Lambda$  mass, nearly identical to the plot for anti- $\Lambda$ .

Figure 3.2: Plot of Decay Length vs  $K_S^0$  mass.

Figure 3.3: Plot of Decay Length Vs. Anti-Lambda Mass – cut was made at the same line as the Lambda cut

Figure 3.4: Number of Detector Hits for the Negative Daughter of the Lambda Mass

Figure 3.5: Number of Detector Hits for the Positive Daughter of the Lambda Mass

Figure 3.6: Number of Detectors Hits vs the Negative Daughter of the Anti-Lambda

Figure 3.7 Number of Detector Hits vs the Positive Daughter of the Lambda

Figure 3.8: Number of Detector Hits vs the Positive Daughters of the  $K^0$  Mass

Figure 3.9: Number of Detector Hits vs the Negative Daughter of the  $K_0$  Mass

Figure 3.10: Illustration for Distance of Closest Approach Cuts

Figure 3.11: DCA cuts for the Lambda Daughters, the negative daughter and the positive daughter.

Figure 3.12: Example  $dE/dx$  plot for demonstrating the necessity of NSigma cuts.

Figure 3.13: Cut was made at plus and minus three for the positive NSigma Proton.

Figure 3.14: Cut was made at plus and minus three for the positive NSigma Pion

Figure 3.15: Cut was made at plus and minus three for the negative NSigma Proton

Figure 3.16: Cut was made at plus and minus three for the negative NSigma Pion

Figure 3.17: Raw Mass Distribution of  $K_S^0$ ,  $\Lambda$ , and anti- $\Lambda$  particles

Figure 3.18: Mass Distribution of Lambda Particle after the application of quality cuts

Figure 3.19: Mass Distribution of Anti-Lambda Particle after the application of quality cuts

Figure 3.20: Mass Distribution of  $K_0$  Particles after the application of quality cuts

Figure 3.21: Mass Distribution of Lambda Particles with Sideband Subtraction

Figure 3.22: Mass Distribution of Anti-Lambda Particles with Sideband Subtraction

Figure 3.23: Mass Distribution of  $K_0$  Particles with Sideband Subtraction

Figure 4.1: Fifteen Lambda Transverse Momentum Bins

Figure 4.2: Fifteen Anti-Lambda Transverse Momentum Bins

Figure 4.3: Lambda Transverse Momentum Spectrum

Figure 4.4: Anti-Lambda Transverse Momentum Spectrum

Figure 4.5: Lambda Transverse Momentum Spectrum with Fit

Figure 4.6: Anti-Lambda Transverse Momentum Spectrum with Fit

Figure 5.1: Plot of Correction Factor for Lambda Particles versus Transverse Momentum for 0-10% Central collisions.

Figure 5.2: Plot of Correction Factor for Lambda Particles versus Transverse Momentum for 10-30% Central collisions.

Figure 5.3: Plot of Correction Factor for Lambda Particles versus Transverse Momentum for 30-60% Central collisions.

Figure 5.4: Plot of Correction Factor for Lambda Particles versus Transverse Momentum for Minimum Bias, all centralities examined.

Figure 5.5: Decay Length of the  $V_0$  for both the embedded and real events.

Figure 5.6: Distance of Closest Approach of the Daughters for both the embedded and real events.

Figure 5.7: Distance of Closest Approach of the Negative Daughter to the Primary Vertex for both the embedded and real events.

Figure 5.8: Number of Detector Hits of the Negative Daughter for real and embedded events

Figure 5.9: Distance of Closest Approach of the Positive Daughters to the Primary Vertex for both the real and embedded data.

Figure 5.10: Number of Detector Hits of the Positive Daughter for real and embedded events

Figure 5.11: Distance of Closest Approach of the VO to the Primary Vertex for real and embedded events

Figure 6.1: Corrected Lambda Transverse Momentum Spectrum with Boltzmann Fit.

Figure 6.2: Anti-Lambda to Lambda Ratio versus Transverse Momentum

Figure 7.1:  $dN/dy$ , or Particle Yield, compared to data from the rest of the world.

Figure 7.2: AntiBaryon/Baryon Ration from experiments around the globe

## List of Symbols and Acronyms

AGS – Alternating Gradient Synchrotron  
 Anti- $\Lambda$  – An anti Lambda particle  
 $\Lambda$  – Lambda particle  
 BRAHMS – One of the other experiments at Brookhaven National Labs  
 $c$  – The speed of light,  $3.0 \times 10^8$  m/s  
 $dN/dy$  – The particle yield for a specific energy  
 $E_t$  – Transverse Energy  
 GeV – Giga Electron Volt  
 GEANT – particle simulator for embedding correction  
 GENTX – particle creator for the embedding correction  
 $K_S^0$  – K0 Short particle, a type of particle created in the collision  
 NA49 – An experiment at SPS  
 NA57 – An experiment at SPS  
 $P_t$  – Transverse Momentum  
 PHENIX - One of the other experiments at Brookhaven National Labs  
 PHOBOS - One of the other experiments at Brookhaven National Labs  
 QGP – Quark Gluon Plasma  
 RHIC – Relativistic Heavy Ion Collider  
 RICH – Ring Imaging Cherenkov Counter  
 SPS – Super Proton Synchrotron  
 STAR – Solenoidal Tracker at RHIC  
 SVT – Silicon Vertex Tracker  
 TPC – Time Projection Chamber



## **Chapter 1: Background and Beginnings**

### **1.1 Understanding High Energy Particle Physics**

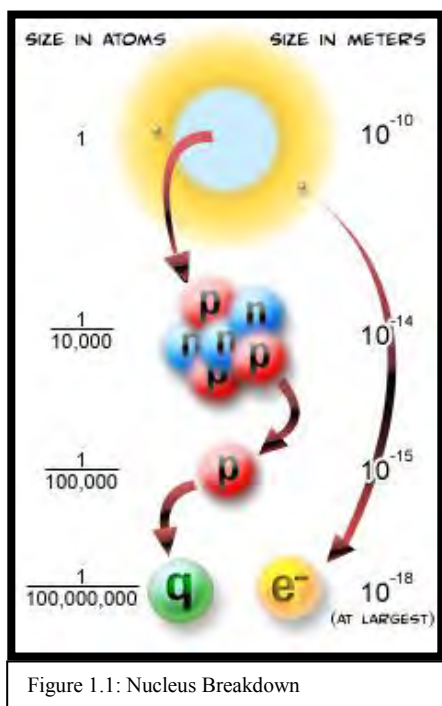
In about 1850, scientists believed that the laws of nature were known to man, and there were only a few exceptions without good explanations. One of these remaining caveats was the existence of an ether, or medium through which light waves pass. Although people disagree on the beginning of the modern physics revolution, many will agree that the Michelson-Morley experiment, proving the non-existence of the ether was the first step towards the knowledge we are gaining today. From Einstein, Bohr, Schrodinger, to Feynman, our knowledge of the world has increased many-fold over the past century, and will only continue to grow. Today experiments and analyses are being done that continue to revolutionize how we understand the world today.

Lately scientists have formed theories about what happened in the creation of the universe after the first three milliseconds. My results provide more information about the dynamics of the first three milliseconds of the universe. As of now, Quark-Gluon Plasma, QGP, is what scientists believe existed at the beginning. QGP is a state of matter where the fundamental particles of nature, quarks, gluons and leptons, exist as a hot and dense plasma at a temperature about 100,000 times hotter than the center of the sun. After about ten microseconds of magnificently fast expansion, the quarks and gluons slowed down enough that they could

begin sticking together.<sup>1</sup> This process is called hadronization. The particles formed in this process, called hadrons, are the particles measured by our detector and are the focus of this analysis.

### 1.1.1. Particle Physics Background

Gaining an understanding of heavy ion collisions that give information about the beginning



of the universe starts with a basic knowledge of fundamental particle physics. The graphic on the left displays the Bohr model of the atom with the nucleus being with electrons orbiting around it. Within the nucleus of the atom exists the nucleons; protons and neutrons. Protons and neutrons can be further broken down into the smallest known particles known to man, quarks. All quarks and anti-quarks are bound together by gluons. Quarks not only make up protons and neutrons, but several other less common particles that are created

in relativistic heavy ion collisions.

There is a complex language to particle physics, but like any other language, one can get by for a few days on just a few words. The first word to learn is “hadron,” a hadron is any type of particle that is formed of quarks. Protons and neutrons are the most common as they make up normal nuclei. The two sub-categories are baryons, which have three valence quarks, and mesons, which are composed of a quark, anti-quark pair.

<sup>1</sup> Michael Riordan and William Zajc, “The First Few Microseconds” *Scientific American*, pg 1, May 2006.

Baryons $qqq$ and Antibaryons $\bar{q}\bar{q}\bar{q}$					
Baryons are fermionic hadrons. There are about 120 types of baryons.					
Symbol	Name	Quark content	Electric charge	Mass $\text{GeV}/c^2$	Spin
$p$	proton	$uud$	1	0.938	1/2
$\bar{p}$	anti-proton	$\bar{u}\bar{u}\bar{d}$	-1	0.938	1/2
$n$	neutron	$udd$	0	0.940	1/2
$\Lambda$	lambda	$uds$	0	1.116	1/2
$\Omega^-$	omega	$sss$	-1	1.672	3/2

Figure 1.2: Well known Baryons and Anti-Baryons

Mesons $q\bar{q}$					
Mesons are bosonic hadrons. There are about 140 types of mesons.					
Symbol	Name	Quark content	Electric charge	Mass $\text{GeV}/c^2$	Spin
$\pi^+$	pion	$u\bar{d}$	+1	0.140	0
$K^-$	kaon	$s\bar{u}$	-1	0.494	0
$\rho^+$	rho	$u\bar{d}$	+1	0.770	1
$B^0$	B-zero	$d\bar{b}$	0	5.279	0
$\eta_c$	eta-c	$c\bar{c}$	0	2.980	0

Figure 1.3: Well known Mesons

Both Figure 1.2 and 1.3 display some of the most well known baryons and mesons of

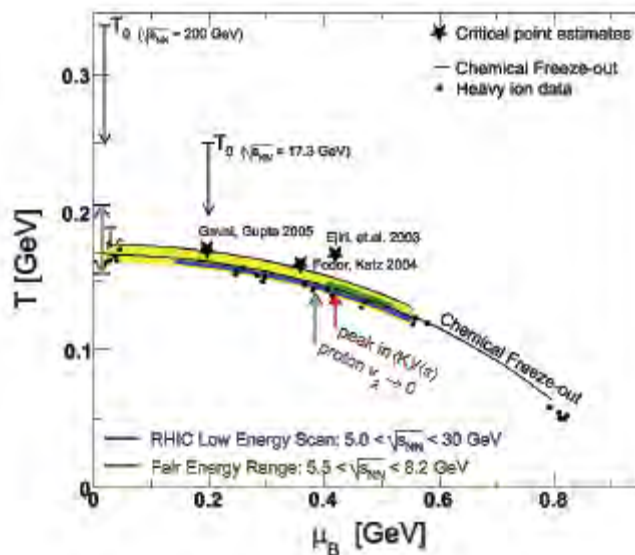


Figure 1.4: Phase Diagram of Nuclear Matter (STAR White Paper 2008)

particle physics. As can be seen in the figures, these particles are composed of various combinations of different quarks. There are currently six known “flavors” of quarks: up, down, top, bottom, strange, and charm.

### 1.1.2. Nuclear Critical Point

One important aspect of understanding a state of matter such as the QGP is to map-out its phase diagram and pin down where a phase transition has occurred and the character of that transition. My results are a step towards greater understanding about the type of transition and the energy at which it occurs. Most of the analysis done today is at 200 GeV collisions, but I am

examining one of the lowest energies at about 19.6 GeV. Several theoretical calculations indicate a first order transition should be expected at slightly higher baryon chemical potentials below those of Super Proton Synchrotron, SPS, that energy ranges from 6.3 to 17.3 GeV in the center of mass.

### 1.1.3. Heavy Ion Collisions

Heavy Ion Collisions at relativistic speeds are some of the most phenomenal scientific experiments ever done. Colliding nuclei at nearly the speed of light are like bags on quarks, waiting to be released upon collision. Coming into these collisions are protons and nucleons from their respective colliding nuclei. When they collide, they form a hot, dense matter, which rapidly expands and sprays particles into the detector. In the detector this experiment looks for particles that contain something other than the up or down quark. For this project, particles that contained strange, s, type quark were analyzed. If a particle that has a strange quark is found, I know for sure is that it originated in the collision. This is because normal nucleons, protons and neutron, do not contain the strange quark. From a collection of particles with strange quarks, an analysis is done to understand what type of matter may have formed these particles.

## 1.2 Brookhaven National Lab and the Relativistic Heavy Ion Collider (RHIC)

### 1.2.1. The Machine

At Brookhaven National Laboratory the Relativistic Heavy Ion Collider, RHIC, was created to study



Figure 1.5: The author and his advisor together with MIDN 3/C Hernandez and LCDR Ita beside the superconducting rings of RHIC

the fundamental properties of particles through ultra-relativistic collisions. In essence, RHIC is the tool used to study QGP, just like a stopwatch is the tool used to measure time. The field of Ultra-Relativistic Heavy Ion research was started in approximately 1980 and is a relatively young field of physics. This experiment is relativistic, because the data being analyzed is from collisions between ions that have been accelerated to near the speed of light. It is described as heavy, because the nuclei used are high in atomic number, typically gold (Au with an atomic number of 79). The ion term indicates that the nuclei have been stripped of all electrons before they are put into the accelerator for collisions. Old nuclear accelerators accelerate nuclei into stationary targets, but RHIC crashes two beams of heavy nuclei into each other creating significantly higher energies. These atomic nuclei reach speeds upwards of 99.99 percent of the speed of light and momenta as high as 100 giga-electron volts per nucleon.<sup>2</sup>

RHIC consists of two 3.8 kilometer rings, and there are a few important steps that the nuclei must go through before they get to the rings (see Figure 1.7). First there is the source of the nuclei which begins the acceleration process. Then the nuclei enter the booster which is a smaller circular accelerator which begins the process of accelerating the nuclei. After that the nuclei go through the Alternating Gradient Synchrotron (AGS), which accelerates them to even higher energies. The AGS energy is effectively 2 to 11 GeV per nucleon. From here the nuclei are split into their respective beams and injected to RHIC itself. The beam lines cross at six different locations around the circumference of the two rings, but at only four of those points do they collide. The four collision points are the four particle detectors, called BRAHMS, PHOBOS, PHENIX, and STAR. These detectors record information about the particles produced in the collisions. 870 superconducting magnets are cooled by tons of liquid helium. These

---

<sup>2</sup> Michael Riordan and William Zajc, "The First Few Microseconds" *Scientific American*, pg 5, May 2006.

magnets direct the beams of particles around the rings and into each other.<sup>3</sup> Through the rings there are several magnets that are used realign and focus the nuclei into a straight line, the rest of the magnets are used to accelerate the nuclei around the rings.

Colliding gold nuclei bring a maximum of 20,000 GeV into an exceedingly small and dense space. Each proton or neutron inside the gold nucleus can reach up to 100 giga-electron volts (GeV). This small and dense space is in essence a fireball which is at its largest the size of a gold nucleus, and approximately three times denser than normal nuclear matter. The protons and neutrons which make up the nucleus of the atoms break down into their fundamental particles, quarks, antiquarks, and gluons.

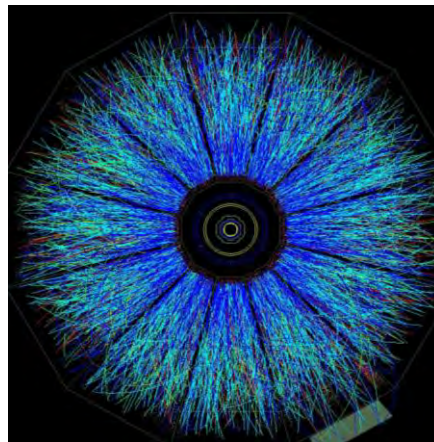


Figure 1.6: Beam Line View of a single Au-Au Collision in STAR

---

<sup>3</sup> Michael Riordan and William Zajc, “The First Few Microseconds” *Scientific American*, pg 5, May 2006.

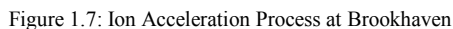


Figure 1.7: Ion Acceleration Process at Brookhaven

The collisions must be categorized to allow systematic study. The broadest category is centrality, a measure of the overlap between colliding nuclei. Centrality is determined by how many particles are created in a collision. If a collision has high centrality it means that the two nuclei hit each other directly head on. A real world example of a very central collision comes from the pool table. A collision with low centrality means that the gold nuclei barely skimmed each other and only a few fundamental particles are created. On the pool table a collision between two balls that has poor centrality would result in a cut shot and a rebound at a different angle.

Immediately after the collision occurs, the fundamental particles recombine (hadronization) into many other particles, such as the  $K_S^0$ ,  $\Lambda$ , and anti- $\Lambda$ 's studied in this project.

The subscript “s” stands for K0 short, a type of particle. Another type of particle is the  $K_L^0$  and it has a lifetime that is two orders of magnitude longer, hence the “L” for long and the “s” for short.<sup>4</sup> These particles and their decay products shoot out into the detector. In this study we examined three different results for the different centralities that were examined. The different bins are 0-10% central, 10-30% central, 30-60% central, and minimum bias, which is a sum of all centralities. If a collision is 0-10% central then the nuclei just barely skimmed each other and there will not be as many particles produced. 30-50% centrality means that we expect more particles to be produced.

### 1.2.2. The Solenoidal Tracker at RHIC (STAR) and the Time Projection Chamber (TPC)

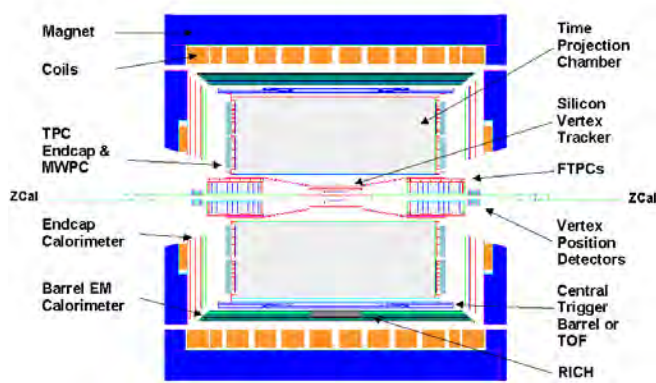


Figure 1.8: Cross-Section of the STAR Experiment

The Solenoidal Tracker at RHIC (STAR) is one of the two largest experiments at RHIC, both in size and in number of scientists. STAR is a large acceptance experiment which has numerous detectors (see Figure 1.8).

The two types of detectors are those that indicate an interaction has

occurred and those that track and measure the particles created in a collision. Each detector subsystem provides information on a different aspect of the particles produced in the collision.

The most important detector for my project is the large Time Projection Chamber, TPC, situated inside a hefty 0.5 Tesla solenoid magnet. The TPC is a tracking detector. It provides information

<sup>4</sup> Particle Data Group, *Particle Physics Booklet* (Extracted from the Review of Particle Physics C. Amsler, *et al.*, Physics Letters B667,1, 2008), 106.



on charge, momentum, and energy loss of charged particles. Other detectors in STAR are the RICH (Ring-Imaging Cherenkov Counter), the Silicon Vertex Tracker (SVT), and two forward Time Projection Chambers (FTPC's).<sup>5</sup> The TPC is the most important because of its high resolution tracking and large acceptance of particles. Its ability to measure energy loss also makes particle identification possible. It is a cylindrical gas-filled tracking chamber 4.2m in length and 4m in diameter. It has an inner radius of .5m and extends to 2m in length.<sup>6</sup> Within this volume is P10 gas which is a mixture of 90% Ar and 10% CH<sub>4</sub>. This gas is used for three important reasons. One is that it has a low level of transverse and longitudinal diffusion allowing high quality track separation. The gas also has an electron drift velocity of about .05m/ $\mu$ s in an electric field greater than 300V/cm and works at atmospheric pressure. At the center of the TPC

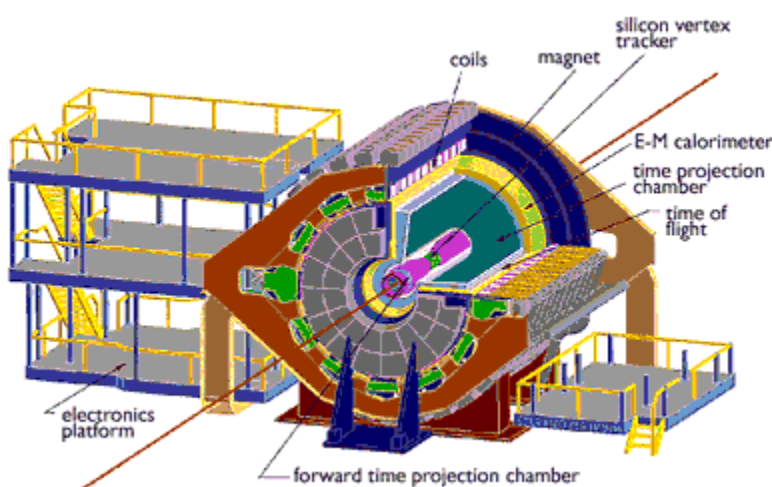


Figure 1.9: The STAR Detector

is a thin cathode maintained at a high voltage of -31000 Volts.

The purpose of the membrane is to create a longitudinal electric field between the center of the TPC where the membrane is located and the ends of the TPC which are held at ground potential. Field cages surround

the volume of the cylinder to keep a uniform electric field.

<sup>5</sup> Matthew A.C. Lamont, "Neutral Strange Particle Production in Ultra-Relativistic Heavy Ion Collisions at 130 GeV." *Thesis for PhD*. University of Birmingham, January 2002, pg 49.

<sup>6</sup> Matthew A.C. Lamont, "Neutral Strange Particle Production in Ultra-Relativistic Heavy Ion Collisions at 130 GeV." *Thesis for PhD*. University of Birmingham, January 2002, pg 49.

The solenoidal magnet in which the TPC sits creates a magnetic field in the volume parallel to the electric field produced from the membrane. The magnetic field causes charged particles to follow helical trajectories. The transverse momentum (meaning perpendicular to the beam lines) of the particles can then be found by calculating the radius of curvature using this equation:

$$P_t = 0.3qBR$$

$R$  represents the radius of curvature of the particle,  $B$  is the magnetic field strength,  $q$  is the charge of the particle, and  $P_t$  is the transverse momentum.<sup>7</sup>

The way we are able to reconstruct collision events is a process of evaluating the ionization of the gas due to the passage of charged particles from the collision. When charged particles travel through the TPC, they ionize the gas producing secondary electrons. These electrons move or drift towards one end of the TPC under the influence of the electric field, created by the cathode membrane at the center and the ends of the TPC held at ground potential. The end of the drift volume is known as the gating grid or the ground plane.

Once the electrons reach the end of the volume or the gating grid they are accelerated towards a grid of anode wires which are held at 1265V. The resulting acceleration of the drifting electrons then causes further ionization of the gas. This ionization creates more electrons and these electrons are also accelerated towards the anode wires. In essence, this process results in an avalanche of electrons on the anode grid. More importantly the drift of positive ions created induces a charge on the cathode plane. The cathode plane is divided up into individual pads and is behind the anode grid. There are 45 pad rows in each sector, therefore giving us 5690 pads and

---

<sup>7</sup> Matthew A.C. Lamont, "Neutral Strange Particle Production in Ultra-Relativistic Heavy Ion Collisions at 130 GeV." *Thesis for PhD*. University of Birmingham, January 2002, pg 52.

about 137,000 readout channels in the Time Projection Chamber. This final ionization is proportional to the initial ionization from the collision particle.

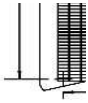


Figure 1.10: A Super Sector of the TPC

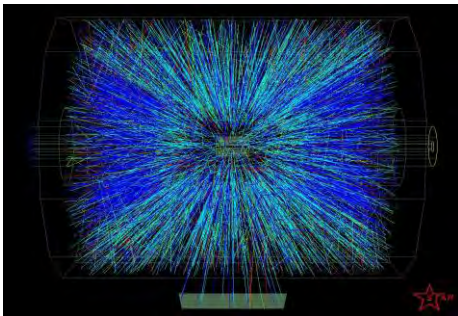


Figure 1.11 : Side View of a Reconstructed Au+Au Collision

Each end wheel of the TPC is comprised of twelve super-sectors (see Figure 1.10). These super-sectors each have an inner and an outer sector of cathode pads. They are mounted into the end cap of the TPC as shown in the cutaway diagram of the TPC (Figure 1.9). The inner sector of the cathode plane has 13 rows as shown in the diagram directly above. There are 32 pad rows in the outer sector. The pads in the inner sector are smaller than the pads in the outer sector and are 2.85mm by 11.5mm. These inner sector pads provide quality two-track spatial resolution in the important regions of the TPC.

These regions are the high density particle regions which are closest to the vertex of the interaction. The spatial representation at these points is important because the particle tracks are very close together in this region. On the other hand the outer pads are larger (6.2mm by 19.5mm) and are optimized for energy loss measurements in the lower track density region. This allows for good particle identification. In summation we are able to get spatial representation near the vertex of the collision where it is most important and we are able to get quality particle identification in the outer fringes of the TPC where that information is most accessible. The charge that is collected in each pad is then broken down into a possible 512 time bins and gives us a total of 70 million pixels in the TPC volume.<sup>8</sup> This is where the TPC gets its name.

Because the beams of ions are moving so incredibly fast there are approximately ten thousand crossings every second but the recording rate for the STAR experiment is limited to 800Hz due to limitations with the readout of the TPC. This means that we need to select the best collisions to use for our data collection, the collisions need to meet certain trigger criteria. Many of the collisions between the beams of ions occur at large impact parameters, or low centrality; therefore not all of the nucleons in the gold nuclei participate in the interaction. These are non-central collisions. Central collisions are where we expect that QGP will most often be formed.<sup>9</sup> We try and have triggers to collect data that will provide good events for analysis. This information is the charge, momentum, and energy loss per unit length for each charged particle.

---

<sup>8</sup> Matthew A.C. Lamont, "Neutral Strange Particle Production in Ultra-Relativistic Heavy Ion Collisions at 130 GeV." *Thesis for PhD*. University of Birmingham, January 2002, pg 54.

<sup>9</sup> Matthew A.C. Lamont, "Neutral Strange Particle Production in Ultra-Relativistic Heavy Ion Collisions at 130 GeV." *Thesis for PhD*. University of Birmingham, January 2002, pg 55.

### 1.2.3. Geometry of Collisions

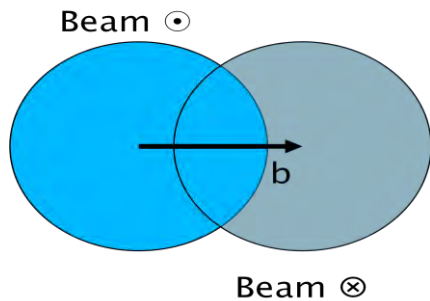


Figure 1.12 : Description of Impact Parameter

In a collision there are a few geometrical terms to keep in mind. Impact parameter is the distance between the centers of the two colliding nuclei. In figure 1.12 it is shown by the line “b”. The reaction plane is the 2D plane where the collision occurs and is akin to the plane formed by the x and z axis in the figure below.

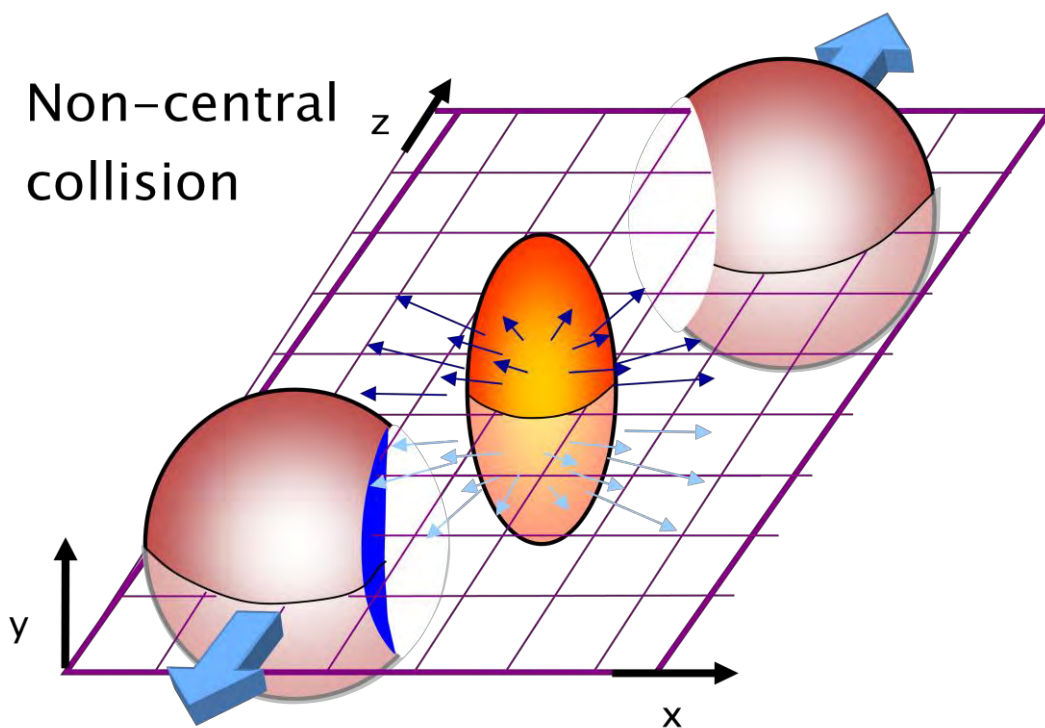


Figure 1.13: Image of a Non-central collision.

## Chapter 2: Initial Data Processing

### 2.1 Raw Mass Distribution

The first step in this analysis is to create a raw mass distribution. In this case raw refers to the sense that the data have yet to be corrected for detector efficiencies. The detector collects information from all the particles. Again the importance of centrality emerges because more central collisions will produce many more particles than collisions that are peripheral. We expect that the number of produced particles (also referred to as multiplicity) in any one event will scale uniquely with the number of participants.<sup>10</sup> Furthermore, we can extend this idea to the concept of transverse energy,  $E_t$ . In this case transverse is defined as the direction perpendicular to the beam. As mentioned before the collisions that occur at RHIC have much more energy than any other experiment previous to it because in all previous experiments the beam has collided with a stationary target, while at RHIC the beams hit each other.

The first step in the analysis is to create raw mass histograms. Once these are created, the background is then reduced to give us the real  $K_S^0$ ,  $\Lambda$ , and anti- $\Lambda$  particles. The particles are then broken up into transverse momentum. The curve is corrected for detector efficiencies and is fitted with a Boltzmann curve. Nevertheless, the initial step in the research is to create the raw mass histograms.

### 2.2 Event Level Cut

The first step done in this analysis is to select only the events that have a uniform acceptance in the TPC. We select only events with a Primary Vertex Position within 50 cm of the

---

<sup>10</sup> Jeffrey T. Mitchell, "RHIC and the Pursuit of Quark-Gluon Plasma" *BNL-68850 Informal Report*, July 25, 2001, pg7.

center of the detector along the beamline. In this way, the selected events have equal amounts of detector in both directions along the beam. The events are created as a part of the reconstruction chain described earlier. The following figure is a histogram of the total number of events vs. the Primary Vertex Position. The events outside 50 cm were not included in the final results. The large spikes just outside the 50 cm mark on both sides of the figure are due to secondary interactions in cooling manifolds for the silicon vertex tracker.

### Primary Vertex Z Position (Before Z Cut)

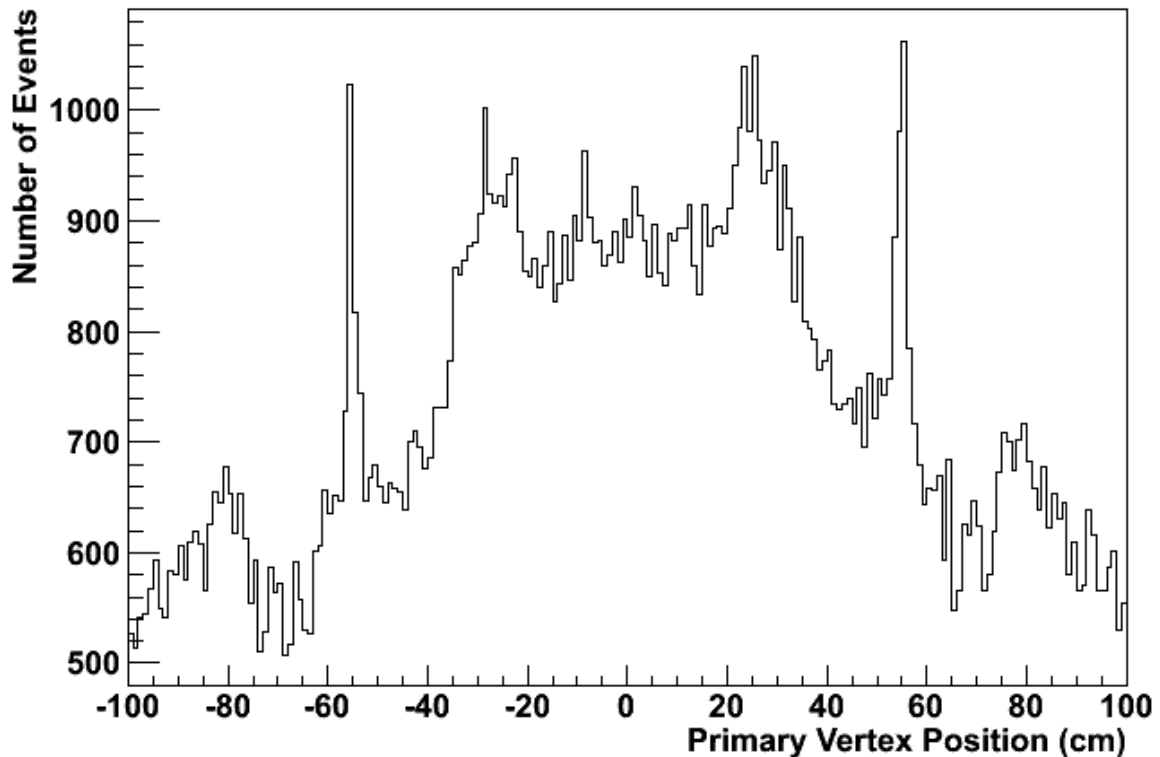
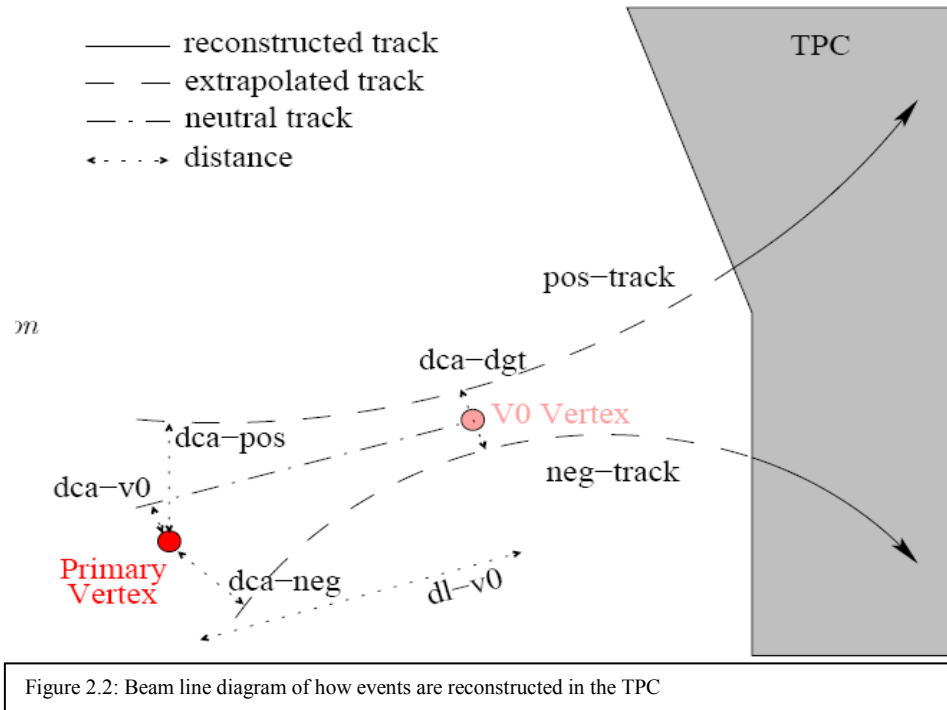


Figure 2.1: Histogram of the Primary Vertex Position Cut at 50 cm

## 2.3 Creation of the Raw Mass Histogram



In order to create the raw mass histograms, the  $K_S^0$ ,  $\Lambda$ , and anti- $\Lambda$  particles have to be reconstructed. For each charged particle passing through the TPC, the Cartesian x,y, and z components of its momentum are measured. Both  $K_S^0$ ,  $\Lambda$ , and anti- $\Lambda$ 's particles are unstable and decay in a short period of time. Figure 2.1 above shows how V0 candidates are reconstructed in the TPC, knowing their tracks and amounts of momentum. We use the term "V0" because the charge tracks emanating from the decay of the neutral parent have the topological appearance of the letter "V". Regardless, there is a positive track, which represents the positive daughter particle, and there is a negative track, which represents the negative daughter particle. The two daughters are recombined to at the vertex to form the V0 or parent particle. The figures of  $K_S^0$ ,  $\Lambda$ , and anti- $\Lambda$ 's displayed on the next few pages display the expected high level of background which is symptomatic of newly formed raw mass distribution. Each V0 candidate is then added to the appropriate bin in a histogram of invariant mass. Count that is shown in the graphs below



is calculated using conservation of energy and conservation of momentum in the decay process. It is described in the following equation.<sup>11</sup>

$$(M_{v0})^2 = (M_1)^2 + (M_2)^2 - 2(E_1 E_2 - p_1 p_2)$$

In this equation  $M_{v0}$  stands is the mass of the parent particle, i.e.  $K_S^0$ ,  $\Lambda$ , and anti- $\Lambda$ 's. In other words it is the mass of the particle that would have decayed into the daughter particles actually detected by STAR. The subscripts 1 and 2 refer to the decay products or the daughter particles from the original parent. For example, with a  $\Lambda$  particle the typical decay channel is into a proton and a negative pion. The figures displayed below are the raw mass distributions that were built for this project. Figure 2.1 shows the raw mass distribution of  $\Lambda$  particles. There is a slight peak at about 1.115 GeV/c<sup>2</sup>. All of the actual  $\Lambda$  particles will be found in this peak. The next figure shows the anti- $\Lambda$  peak; this histogram shows less of a significant peak than the one for  $\Lambda$  particles. The peak is less pronounced because there are fewer anti- $\Lambda$ 's produced overall. Lastly, the  $K_S^0$  histogram looks different than the ones produced for  $\Lambda$ 's and anti- $\Lambda$ 's. The mass peak for the  $K_S^0$  is not the large bump at the left side of the plot. The bump is part of the combinatorial background. The peak occurs at about .497 GeV/c<sup>2</sup>, the mass of the  $K_S^0$  particle.

In this project we use the term “invariant mass” which is not the same as “rest mass”, as seen in the equation below.<sup>12</sup>  $M_{ab}$  is the invariant mass, while the rest mass is included in the total energy.

$$(p_{au}c + p_{av}c)^2 = (E_a + E_b)^2 - (p_a c + p_b c)^2 = M_{ab}^2 c^4$$

---

<sup>11</sup> Matthew A.C. Lamont, “Neutral Strange Particle Production in Ultra-Relativistic Heavy Ion Collisions at 130 GeV.” *Thesis for PhD*. University of Birmingham, January 2002, pg 74.

<sup>1212</sup> Ernest M. Henley and Alejandro Garcia, *Subatomic Physics*, 3<sup>rd</sup> ed. New Jersey: World Scientific Publishing Co. 2007), 6.

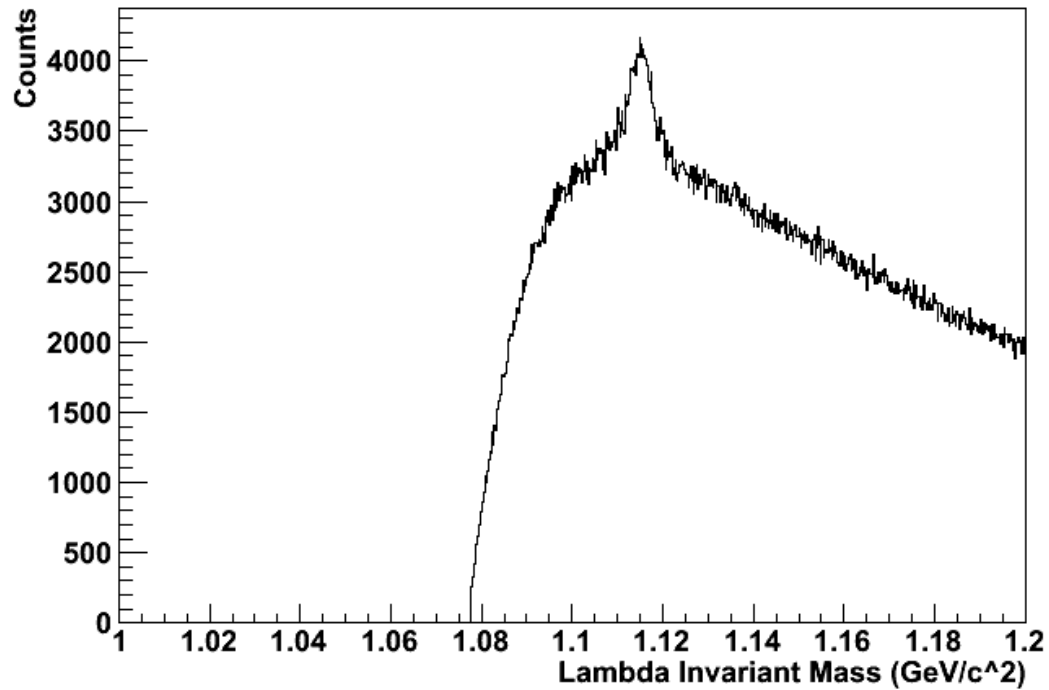
**Raw Mass Distribution of Lambdas, No cuts**

Figure 2.3: Raw Lambda Mass Distribution before any cuts are applied to the data.

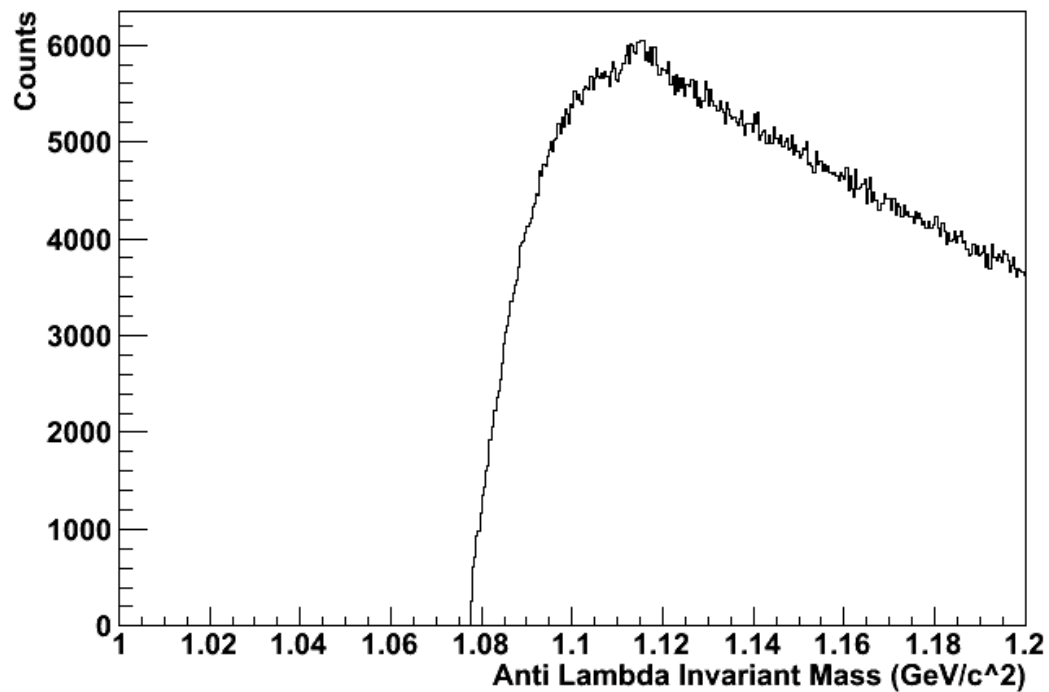
**Raw Mass Distribution of Anti-Lambdas, before cuts**

Figure 2.4: Raw Anti Lambda Mass Distribution before any cuts are applied

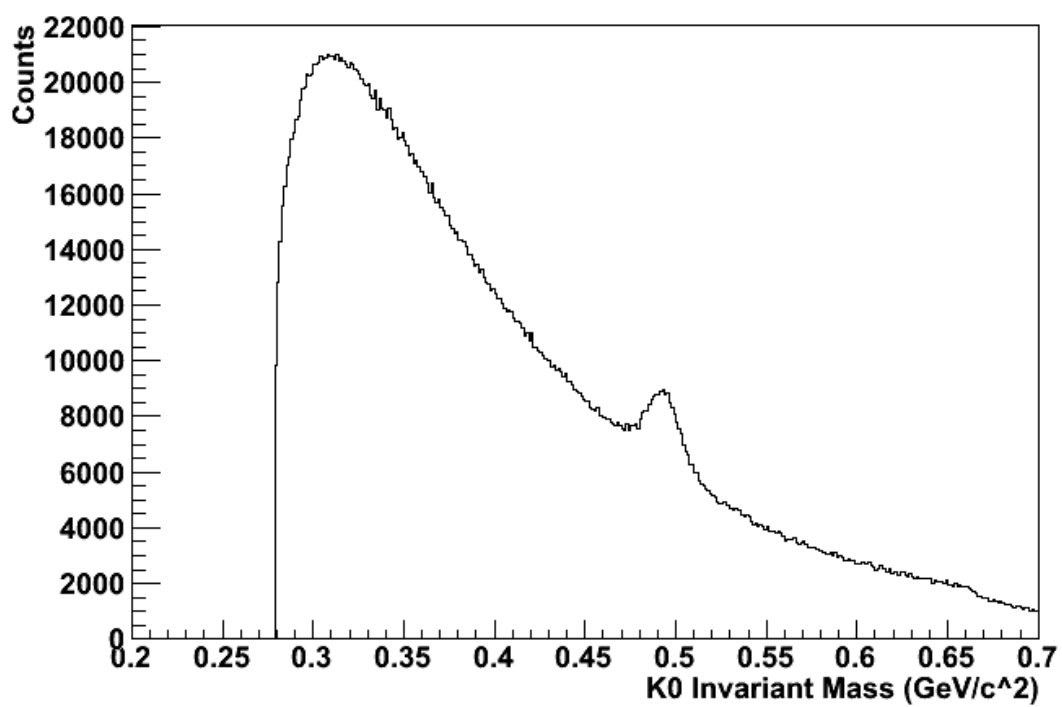
**Raw Mass Distribution of K0s, No cuts**

Figure 2.5: Raw Mass Distribution of K0's particles before any cuts are applied

## Chapter 3: Analysis and Background Reduction

### 3.1 Reducing the Background

Once the raw mass distributions are formed as a combination of two daughter particles, the resulting histograms have a significant level of background. Within these mass distributions exist true  $K_S^0$ ,  $\Lambda$ , and anti- $\Lambda$ 's. The next step is therefore to remove as much of the background as possible so that I am only left with as many true  $K_S^0$ ,  $\Lambda$ , and anti- $\Lambda$ 's as possible. For each of the particles I placed a series of cuts on the candidates. The process by which I choose where the cuts will be placed is called cut tuning. This process requires running over all the events several times while applying different cuts on the data. The chosen set of cuts is used because they resulted in the most optimal signal to background ratio.

#### 3.1.1. Rapidity Cut

For  $K_S^0$ ,  $\Lambda$ , and anti- $\Lambda$ 's the rapidity cut was on the V0 was put at 0.5. For this experiment, rapidity plays the role of relativistic velocity. The cut is applied because the TPC has a uniform response from -0.5 to 0.5 units in rapidity. If a track has a rapidity outside of 0.5 rapidity then it is eliminated mass distribution.

#### 3.1.2. Decay Length of the V0

The decay length of a V0 is a measure of the lifetime of that parent. If it has a longer lifetime, then it is going to take a long time to decay and will consequentially have a long decay length. The decay length cut for the  $K_S^0$ ,  $\Lambda$ , and anti- $\Lambda$ 's was placed at 6 cm. The meaning of this cut is that all  $K_S^0$ ,  $\Lambda$ , and anti- $\Lambda$ 's that remain in the data set must have originated less than or equal to 6 cm from the Primary Vertex of the collision under review. The following figures

illustrate exactly how many particles were removed from the data set from this cut. In figure 3.1 the decay length vs.  $\Lambda$  mass is displayed. The hotter, more red, colors represent higher density of particles. A close examination of the figure shows a denser region of particle concentration around  $1.115 \text{ GeV}/c^2$ , the  $\Lambda$  mass. This is most acutely seen at the higher values of decay length.

**2D Plot of Decay Length Vs Lambda Mass**

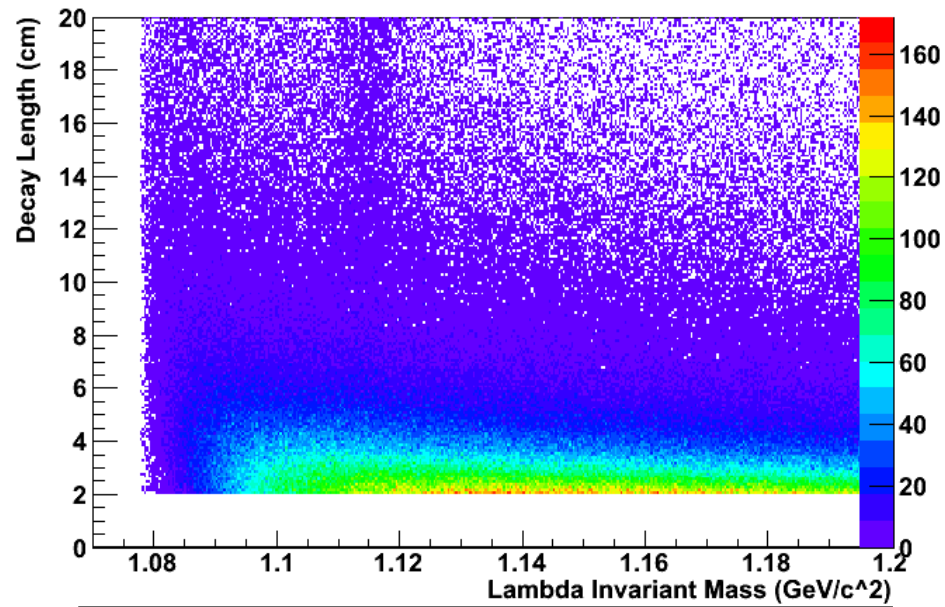


Figure 3.1: Plot of Decay Length for the  $\Lambda$  mass, nearly identical to the plot for anti- $\Lambda$ .

2D Plot of Decay Length Vs K0ShortMass

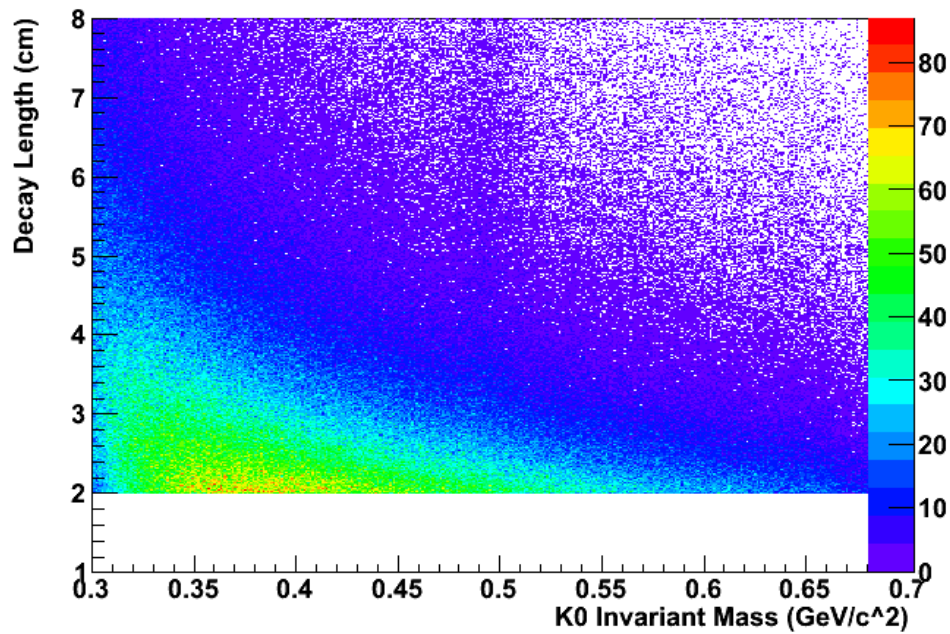


Figure 3.2: Plot of Decay Length vs  $K_S^0$  mass.

2D Plot of Decay Length Vs Anti Lambda Mass

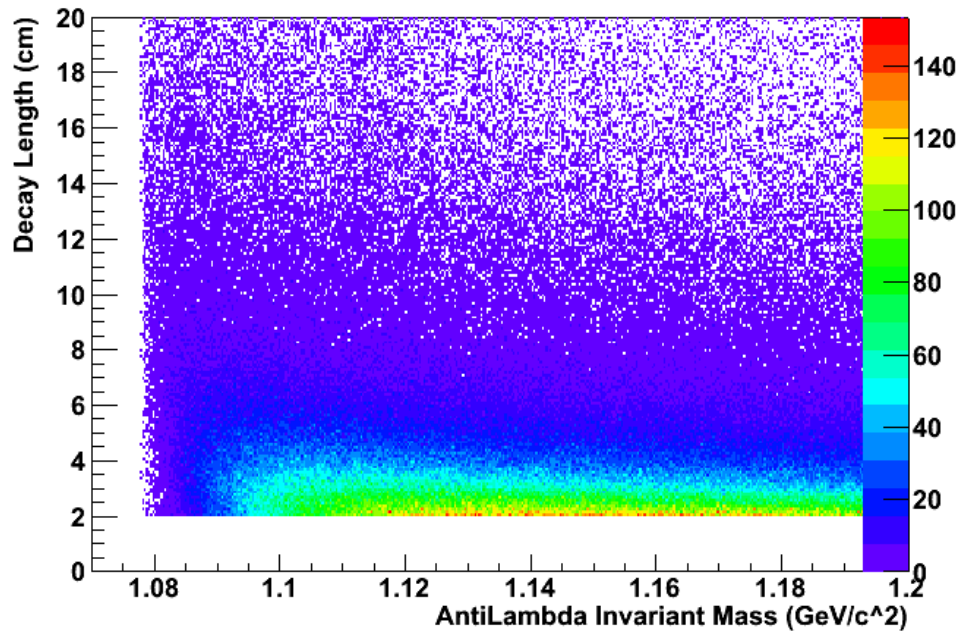


Figure 3.3: Plot of Decay Length Vs. Anti-Lambda Mass – cut was made at the same line as the Lambda cut

A side effect of the decay length cut is that a significant number of real  $K_S^0$ ,  $\Lambda$ , and anti- $\Lambda$ 's will be removed in the cut. This is seen in the figures above. Nevertheless, this is an unavoidable side

effect because the cut will significantly reduce the background. The lost  $\Lambda$ 's and anti- $\Lambda$ 's are corrected for in the correction process at the end of the analysis.

### 3.1.3. Number of Detector Hits

The next cut placed on the data was a limiter on the number of detector hits that could qualify as a track. From chapter one and two, each particle track is a composition of ionization that hits the pad-plane, which segments it into at most 45 hits, one for each pad row. Each particle track is a connected line of a number of points. Each point is equivalent to a cluster of ionization from the gas in the TPC. The validity and integrity of these tracks is improved by cutting on the number of detector hits, longer tracks are higher quality. Both the positive daughter and the negative daughter of the V0 parent particle are subjected to a number of detector hit cuts. Through the process of cut optimization I determined that both the positive and negative daughter number of hits cuts should be placed at 15 hits for the  $K_S^0$ ,  $\Lambda$ , and anti- $\Lambda$ 's. All tracks with fifteen or fewer are removed from the analysis. The cuts are shown below in the following graphs.

2D Plot of N Hits + Daughter Vs Lambda Mass

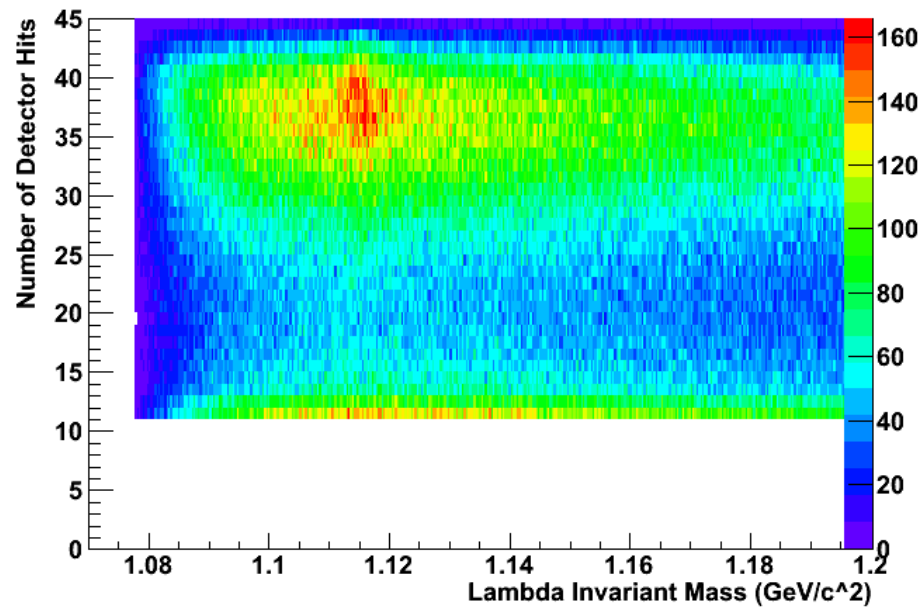


Figure 3.4: Number of Detector Hits for the Negative Daughter of the Lambda Mass

2D Plot of N Hits - Daughter Vs Lambda Mass

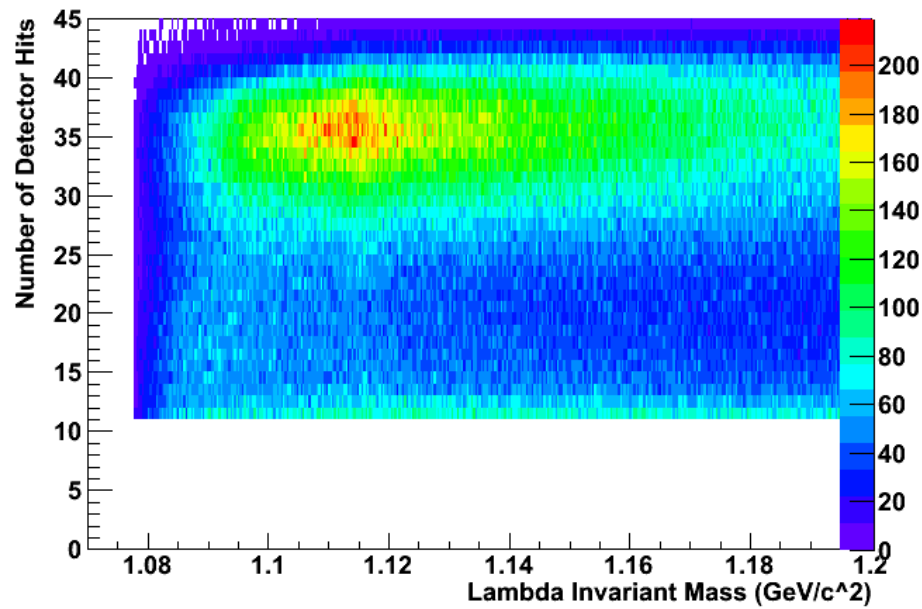


Figure 3.5: Number of Detector Hits for the Positive Daughter of the Lambda Mass



2D Plot of N Hits - Daughter Vs Anti Lambda Mass

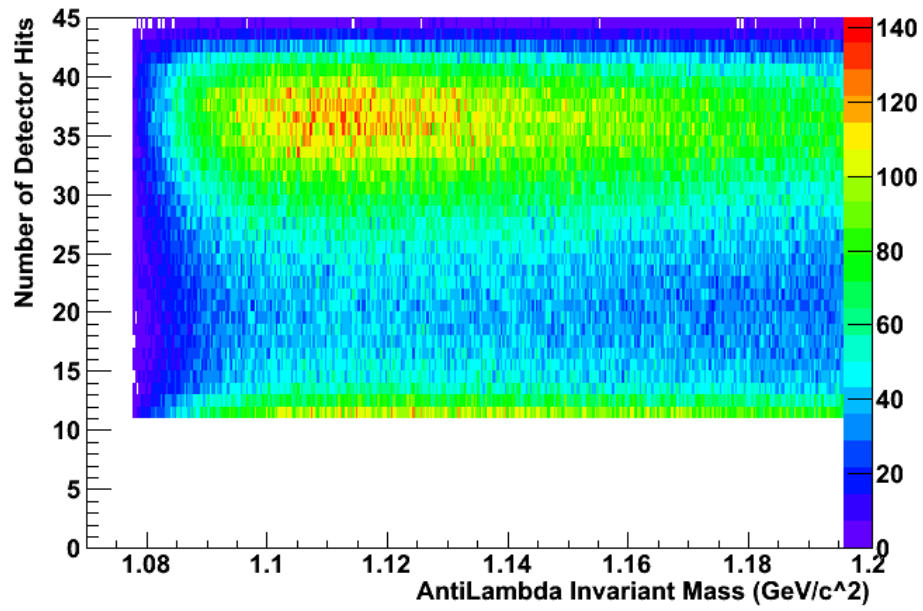


Figure 3.6: Number of Detectors Hits vs the Negative Daughter of the Anti-Lambda

2D Plot of N Hits + Daughter Vs Anti Lambda Mass

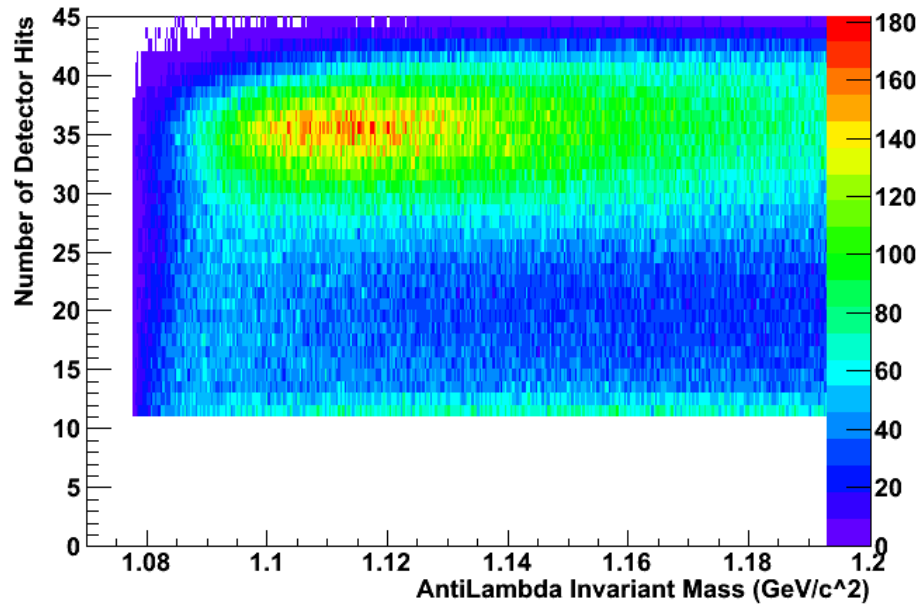


Figure 3.7 Number of Detector Hits vs the Positive Daughter of the Lambda

2D Plot of N Hits + Daughter Vs K0ShortMass

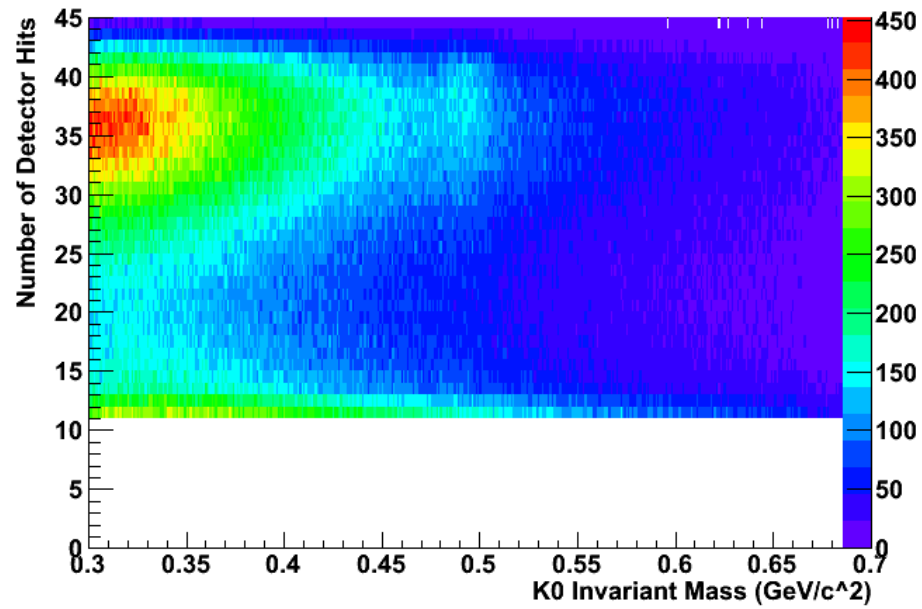


Figure 3.8: Number of Detector Hits vs the Positive Daughters of the K0 Mass

2D Plot of N Hits - Daughter Vs K0ShortMass

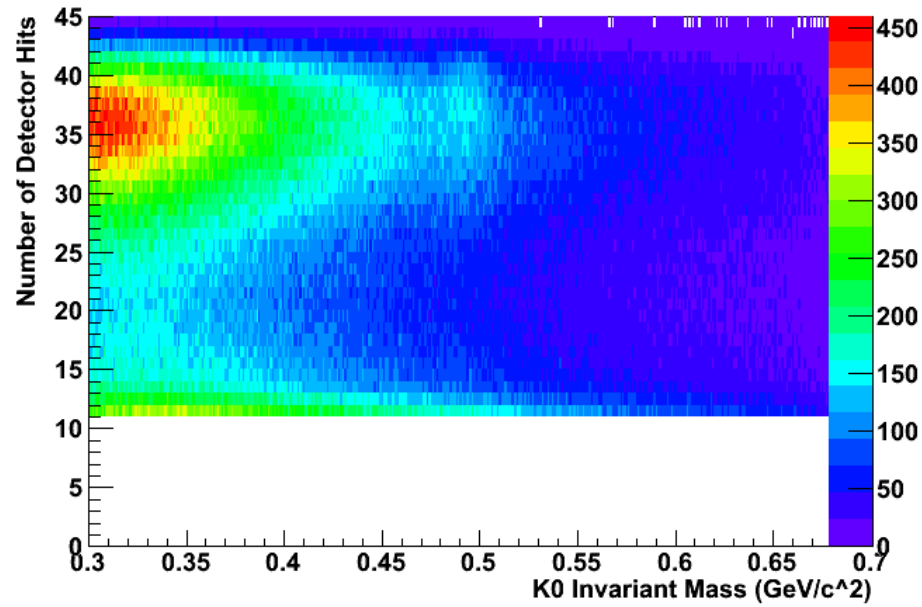
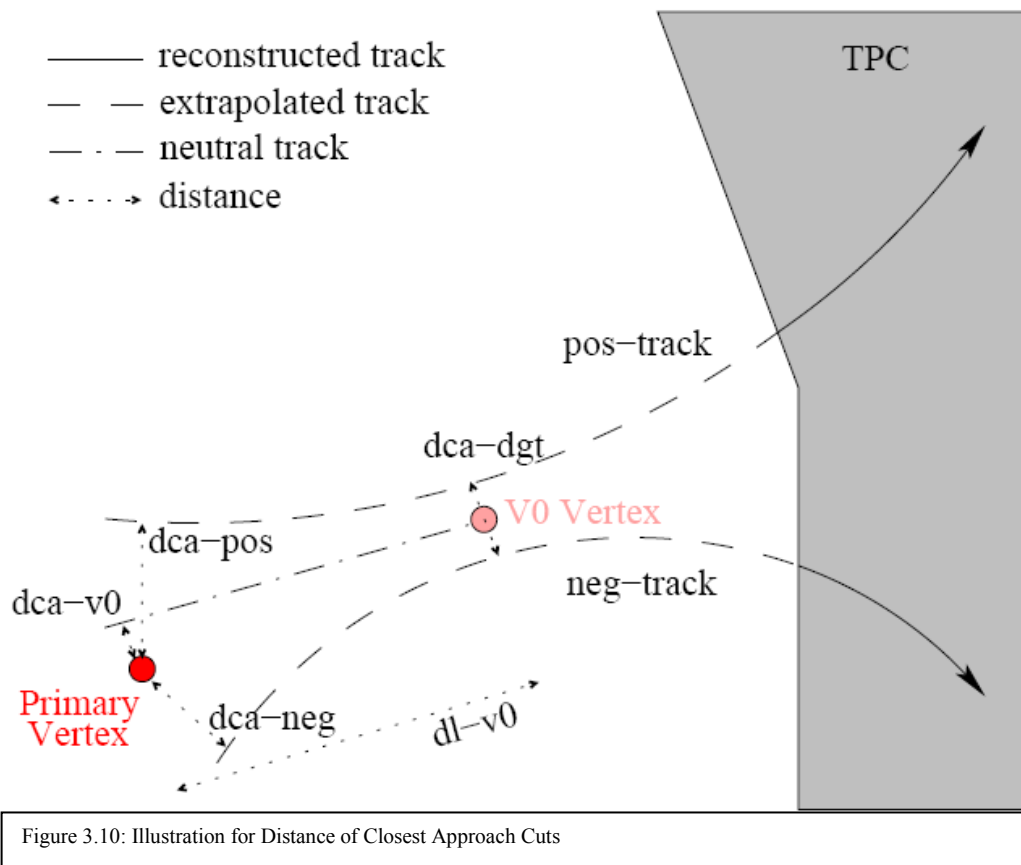


Figure 3.9: Number of Detector Hits vs the Negative Daughter of the K0 Mass

These graphs are two-dimensional plots with hotter colors representing a higher number density of particles. For each of the graphs there are red zones at about forty detector hits for the positive daughter and between thirty-five and forty for the negative daughter. After seeing these plots, I decided to make an initial cut at twenty-five hits, consequentially eliminating all of the tracks below the twenty-five hits line. As I continued optimizing my other cuts, I tried to lower my cut to allow more candidates from twenty-five to twenty and eventually stopping at fifteen. The cut could be made anywhere between twenty-five and fifteen, however the signal to background ratio in this analysis is optimum with the cut at fifteen hits.

#### **3.1.4. Distance of Closest Approach Cuts**

There is a series of several cuts that were taken which deal with the distance of closest approach (DCA) to the primary vertex for the daughter and parent particles. The following diagram is displayed for the second time, yet is a pertinent explanation of the procedure for making cuts on the DCA.



Within the QGP, there are hundreds of protons and pions that are sprayed out into the detector. Not all of these protons and pions are the daughters of  $\Lambda$  particles, and it is necessary to remove the excess protons and pions not from  $\Lambda$  parents.

This diagram has the primary vertex, where the collision occurred, highlighted in red. To the upper right is the V0 Vertex, the point where the V0 parent decayed. The “dca-dgt” is short for the distance of closest approach for the daughters of the V0 decay. For the  $K_S^0$ ,  $\Lambda$ , and anti- $\Lambda$ s this distance was capped at a maximum of .8 cm. In essence, if the component daughter particles did not come within .8 cm of the parent calculated vertex, then the candidate is removed from the raw mass distribution.

The “dca-pos” and the “dca-neg” were two other necessary cuts, but these cuts are a little different. This cut is made by eliminating the daughter particles whose tracks originate near the primary vertex position. If a daughter of a  $\Lambda$ , a proton or a pion, comes from the center of the collision, then it probably did not decay from a parent. The proton or pion was most likely formed in a some other interaction other than a  $\Lambda$  decay. For the  $\Lambda$  mass, any positive daughters that is closer than 1.05 cm to the primary vertex of the collision is cut out. For the negative daughter particles, daughter particles closer than 2.5 cm to the primary vertex position are cut out. Since the anti- $\Lambda$  has daughter particles that are opposite in sign to the  $\Lambda$  particle, the cuts are reversed. The negative daughters closer than 1.05 cm to the primary vertex are removed, while the positive daughters approaching closer than 2.5 cm are removed. The  $K_S^0$  particle has a different set of cuts from the  $\Lambda$  and anti- $\Lambda$  particles. If either the positive or negative daughter is closer than 1.3 cm to the primary vertex, then the particle is removed. By inspection the signal to background was optimized through all of these cuts.

The last cut is represented in the diagram as “dca-v0” which stands for the distance of closest approach of the V0 parent to the primary vertex of the event collision. Parent particles we examine,  $K_S^0$ ,  $\Lambda$ , and anti- $\Lambda$ ’s, all have an average life span before they decay into their daughter particles. These particles exit the QGP at a fast speed, and from their lifetime an estimate of how far into the detector these particles should travel before they decay can be made. If a reconstructed V0 falls a significantly short distance from the primary vertex, it is safe to assume that the particle is not a true  $K_S^0$ ,  $\Lambda$ , or an anti- $\Lambda$ , and therefore it can be removed from the data. For all three of the particles if the V0 distance of closest approach is less than one cm, it is omitted from the mass distribution.

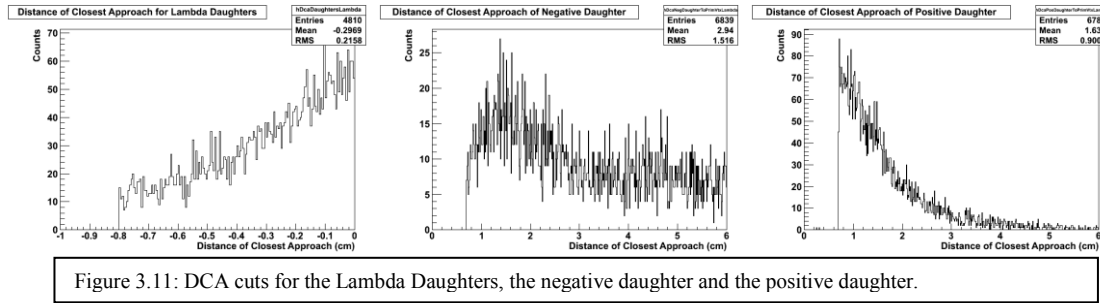


Figure 3.11: DCA cuts for the Lambda Daughters, the negative daughter and the positive daughter.

### 3.1.5. Cut on the NSigma

NSigma is a way of cutting on the particle identification. In the sample graph on the left, there are four different types of particles that are represented.<sup>13</sup>

The red regions of the graph represent high density of particles and the lines represent about where the particles should be if they are real. An NSigma cut

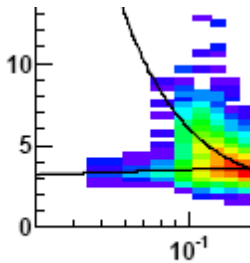


Figure 3.12: Example dE/dx plot for demonstrating the necessity of NSigma cuts.

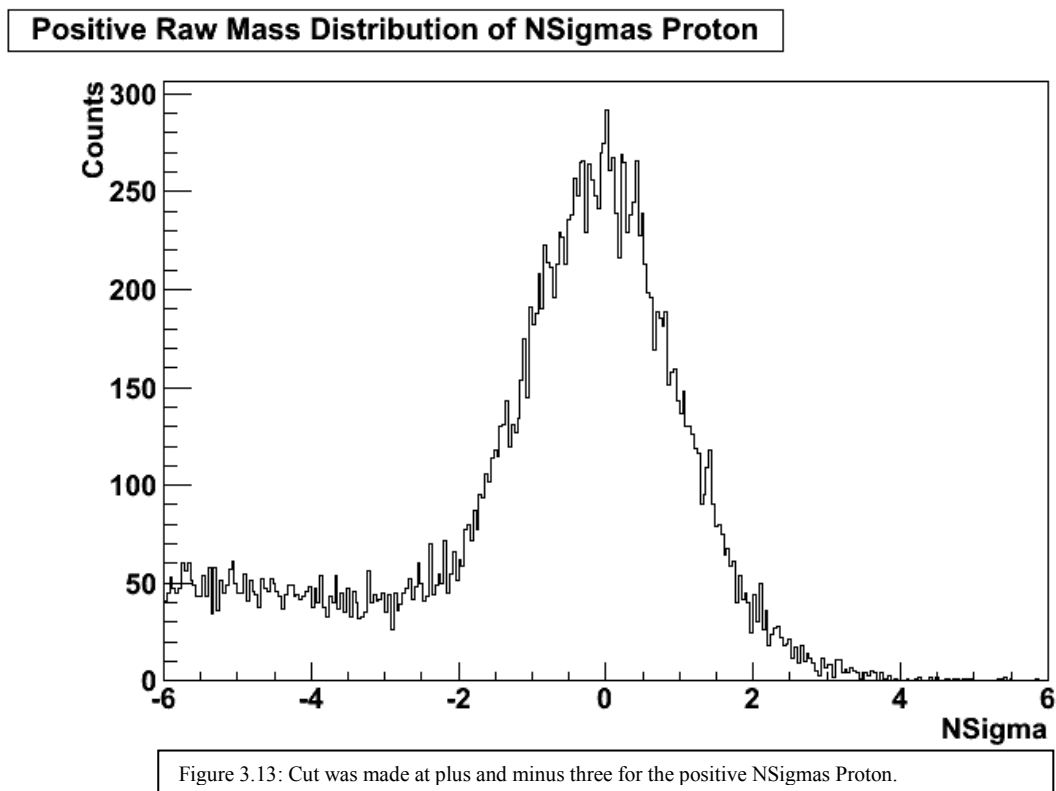
examines the validity of the particles by

removing any of the particles that are more too far away from the average to be real particles.

The “sigma” in my NSigma cut is one standard deviation assuming a Gaussian shape for the peak. By making cuts on the NSigma, the likelihood that a random particle is counted in the  $K_S^0$ ,  $\Lambda$ , and anti- $\Lambda$  peak is reduced. The cut on the NSigmas was made at three for the  $K_S^0$ ,  $\Lambda$ , and anti- $\Lambda$ s. This cut was made on the positive NSigmas proton, the positive NSigmas pion, the

<sup>13</sup> Anthony Timmins, “Neutral Strange Particle Production in Relativistic Cu+Cu Collisions at 200 GeV.” *Thesis for PhD*. University of Birmingham, July 2008, pg 55.

negative NSigmas proton and the negative NSigmas pion. For example, the NSigmas proton could be represented by the black line in figure 3.12. If a candidate is more than three sigma away from the line, it is eliminated. The following histograms properly displayed the sections that were removed from the data. Negatively charged protons are one of the daughter particles of anti- $\Lambda$ s. Figure 3.13 illustrates how rare negatively charged protons, anti-protons, occur. Nevertheless, this data is sufficient for our purposes and nothing more can be done to correct it.



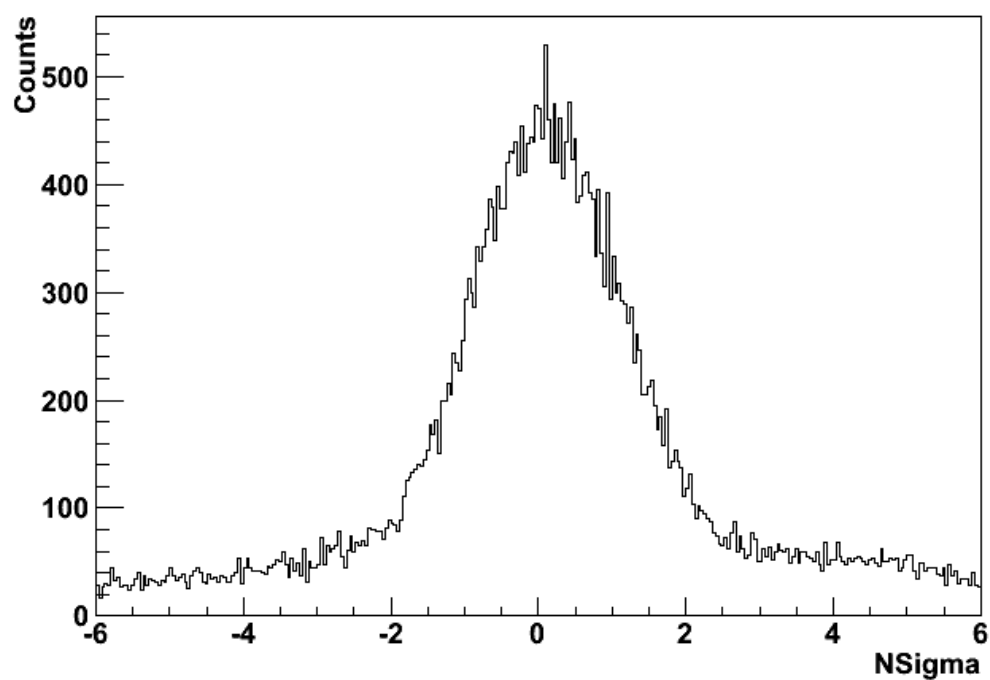
**Positive Raw Mass Distribution of NSigma Pion**

Figure 3.14: Cut was made at plus and minus three for the positive NSigma Pion

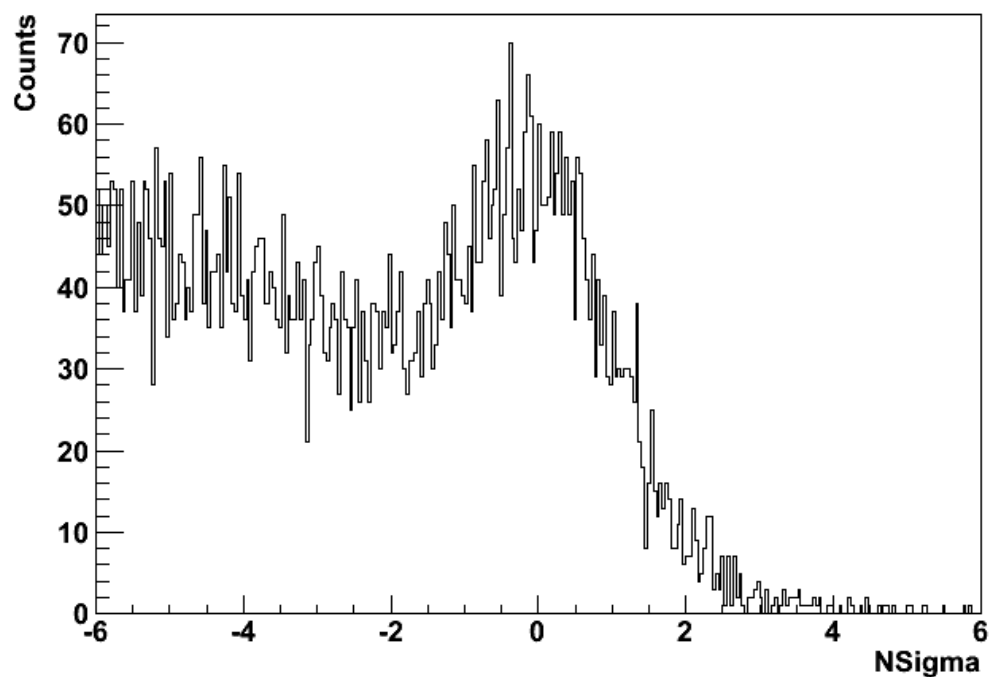
**Negative Raw Mass Distribution of NSigma Proton**

Figure 3.15: Cut was made at plus and minus three for the negative NSigma Proton



### Negative Raw Mass Distribution of NSigmas Pion

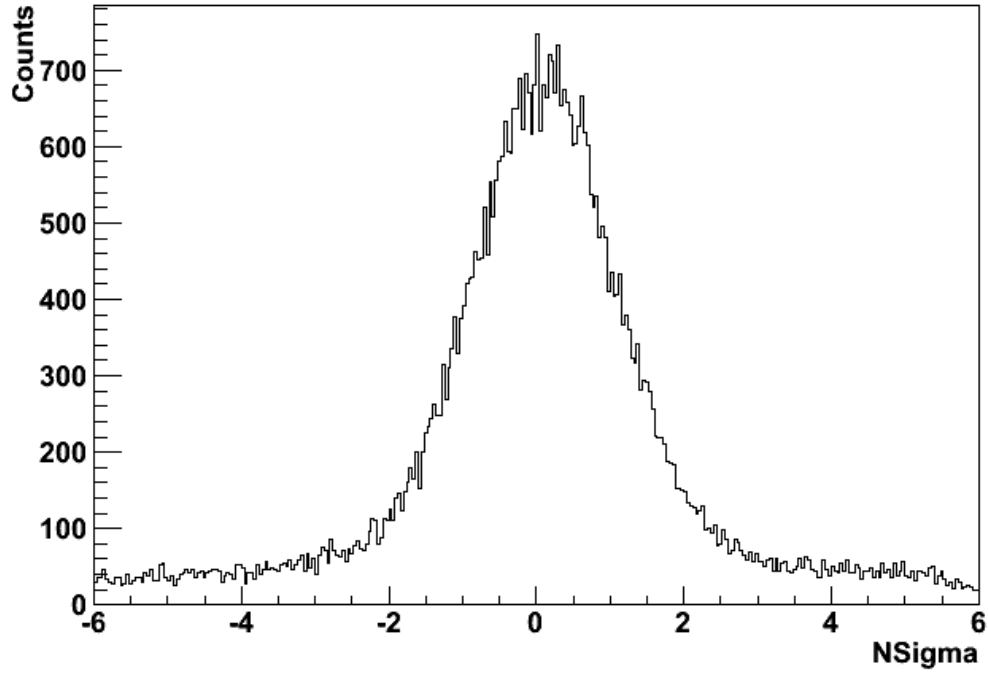


Figure 3.16: Cut was made at plus and minus three for the negative NSigmas Pion

## 3.2 Resultant $K_S^0$ , $\Lambda$ , or anti- $\Lambda$ Histograms

### 3.2.1. Mass Peaks

The purpose of applying several quality cuts was to reduce the background present in the  $K_S^0$ ,  $\Lambda$ , and anti- $\Lambda$  mass distributions. Displayed in the figures below is the raw mass distribution of the  $K_S^0$ ,  $\Lambda$ , and anti- $\Lambda$  particles before cuts.

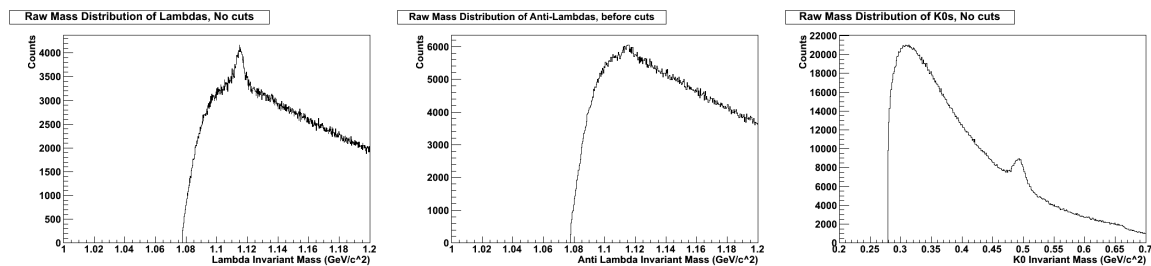


Figure 3.17: Raw Mass Distribution of  $K_S^0$ ,  $\Lambda$ , and anti- $\Lambda$  particles

There is a significant level of background and the peaks are not pronounced. The following three figures show the results of the quality cuts.

### Raw Mass Distribution of Lambdas

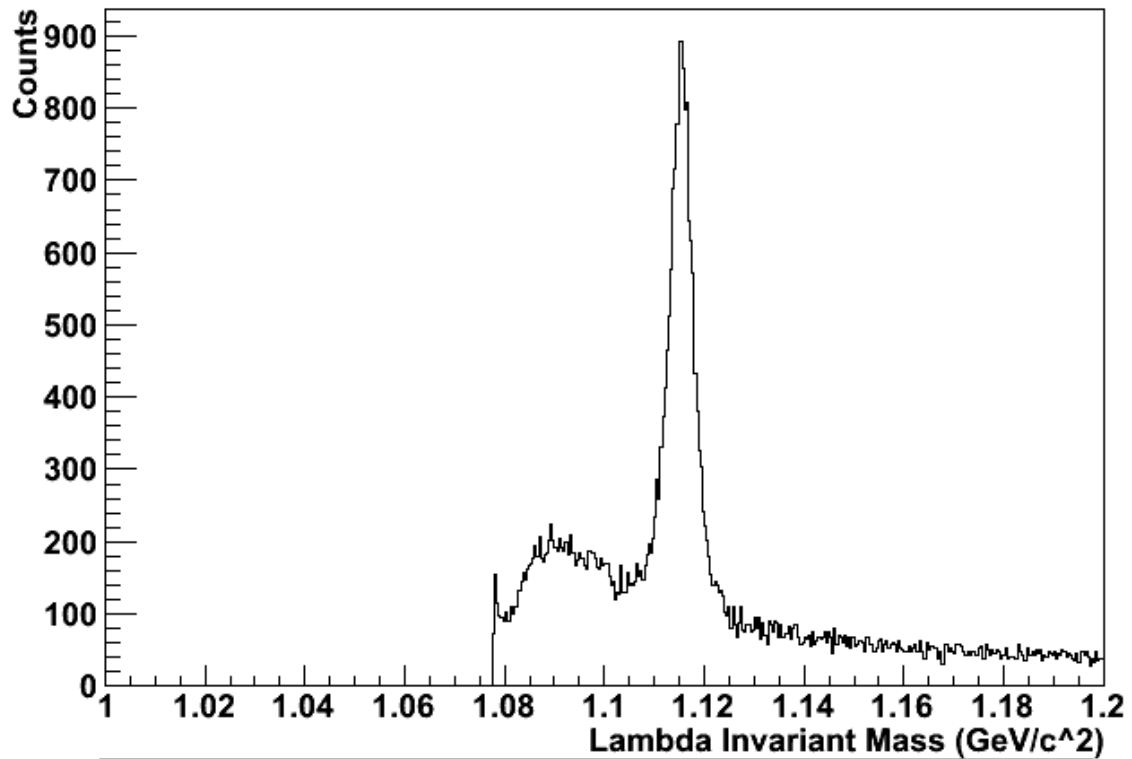


Figure 3.18: Mass Distribution of Lambda Particle after the application of quality cuts

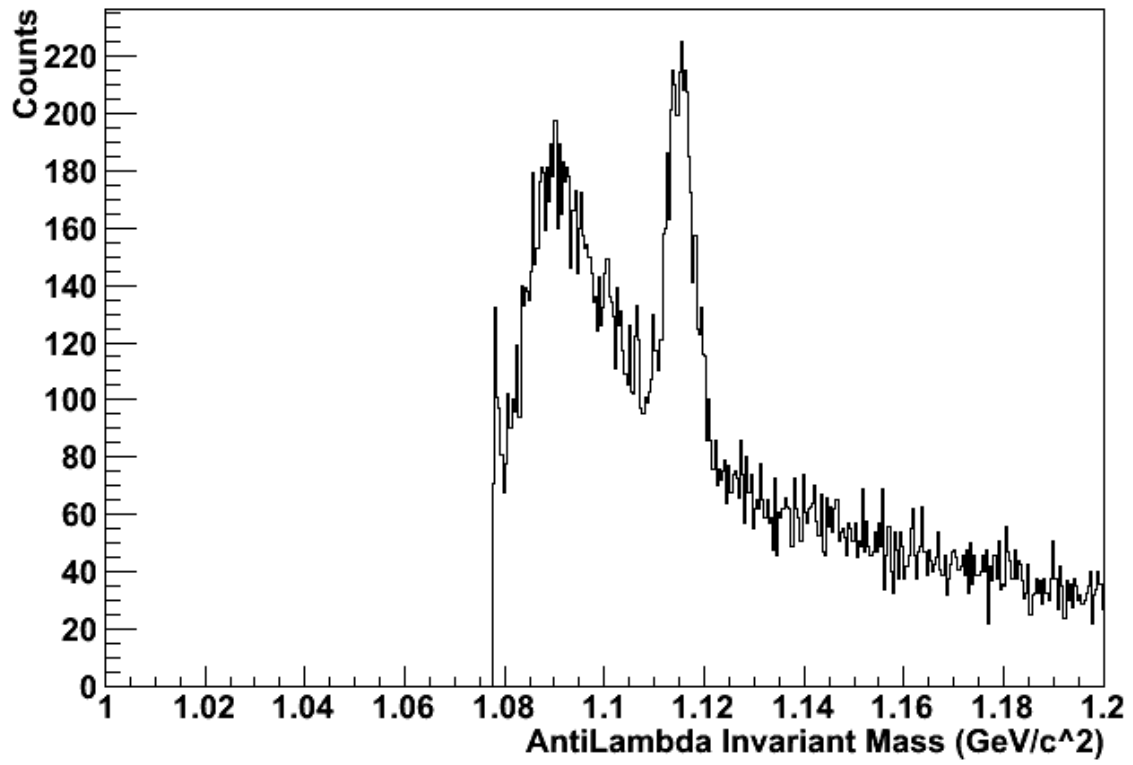
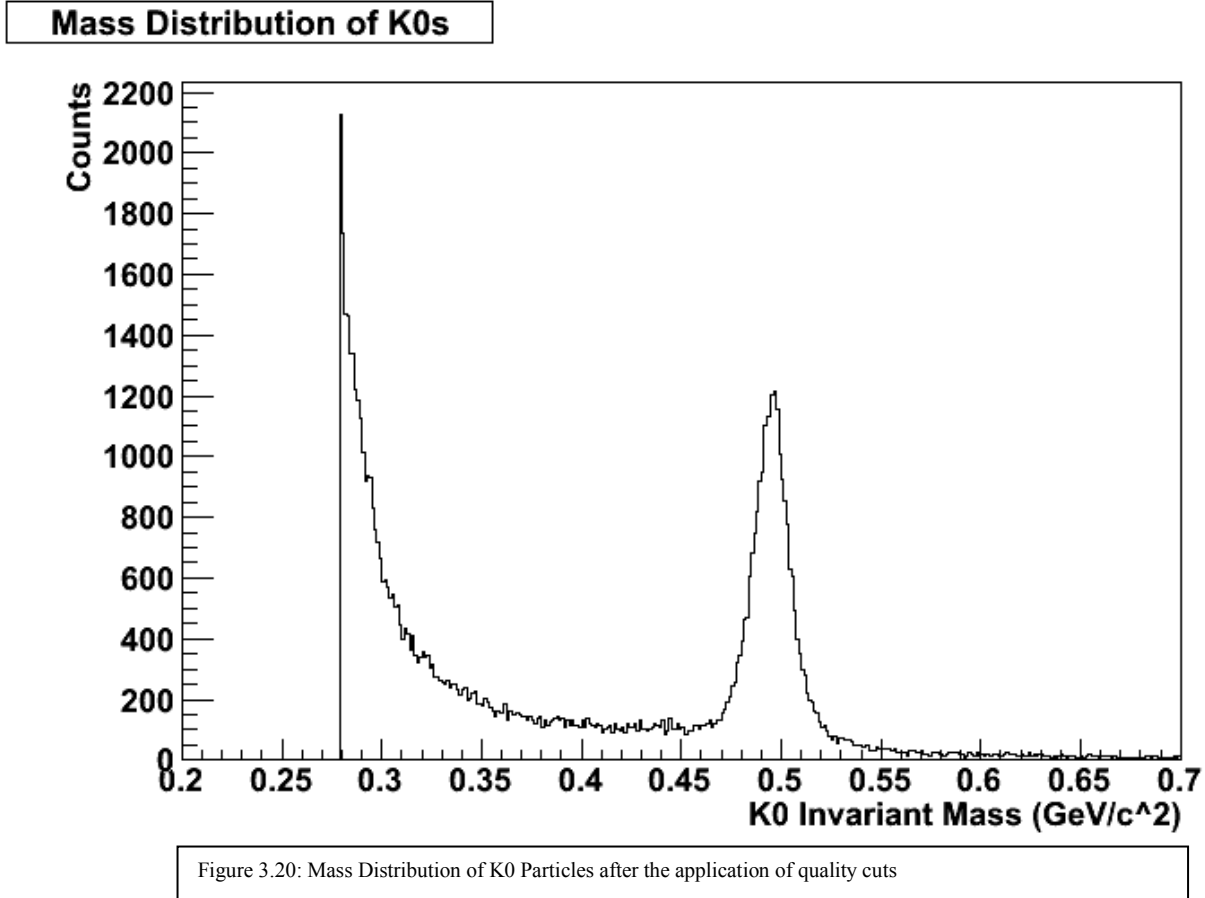
**Distribution of Anti Lambdas**

Figure 3.19: Mass Distribution of Anti-Lambda Particle after the application of quality cuts

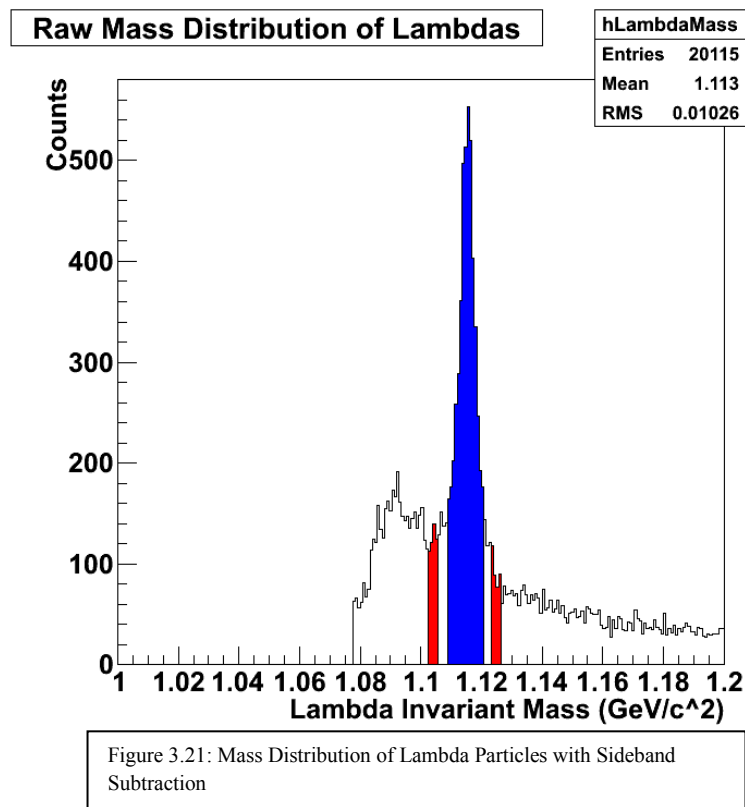


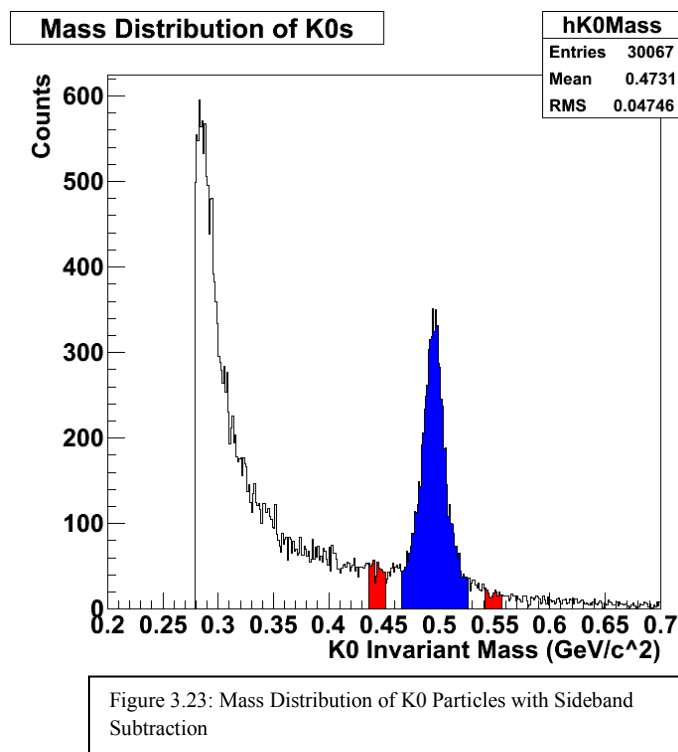
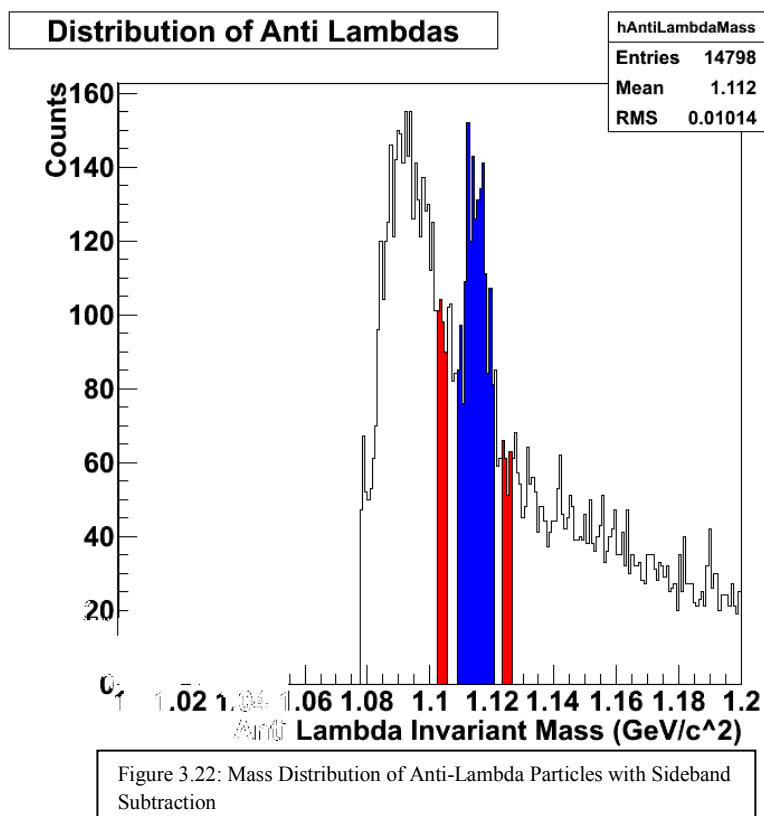
These distributions for the  $K_S^0$ ,  $\Lambda$ , and anti- $\Lambda$  particles show pronounced mass peaks at the accepted masses for each of the particles. The quality cuts significantly reduced the background; inevitably there were several true  $K_S^0$ ,  $\Lambda$ , and anti- $\Lambda$  particles that were removed in the cuts. This is acceptable for the importance of the high optimization of the signal to background ratio.

### 3.2.2. Bin Counting and Sideband Subtraction

The next step in the data analysis is to account for the remaining residual background. This can be done through a process of bin counting and sideband subtraction. The following figures illustrate the process through which sideband subtraction takes place.

In each of the final mass distributions, in the top right corner, a key exists that explains some information about the histogram. Entries is simply the number of counts or particles total in the histogram. Mean is the average invariant mass over the whole histogram. RMS stands for root mean square which is a way of describing the sharpness of the peak. The smaller the RMS the sharper the peak.





In these graphs there are two main sections, the signal mass peak is highlighted in blue and each are four sigma wide. The regions shown in red are the parts that were subtracted. An average was taken between the two heights of the red region. From those two points, an average background was calculated.

$$(\text{Red Region 1} + \text{Red Region 2}) / 2 = \text{Average Background}$$

This average background value was then subtracted from the blue mass peak leaving me with a final mass peak. It is with this mass peak that further analysis is completed.

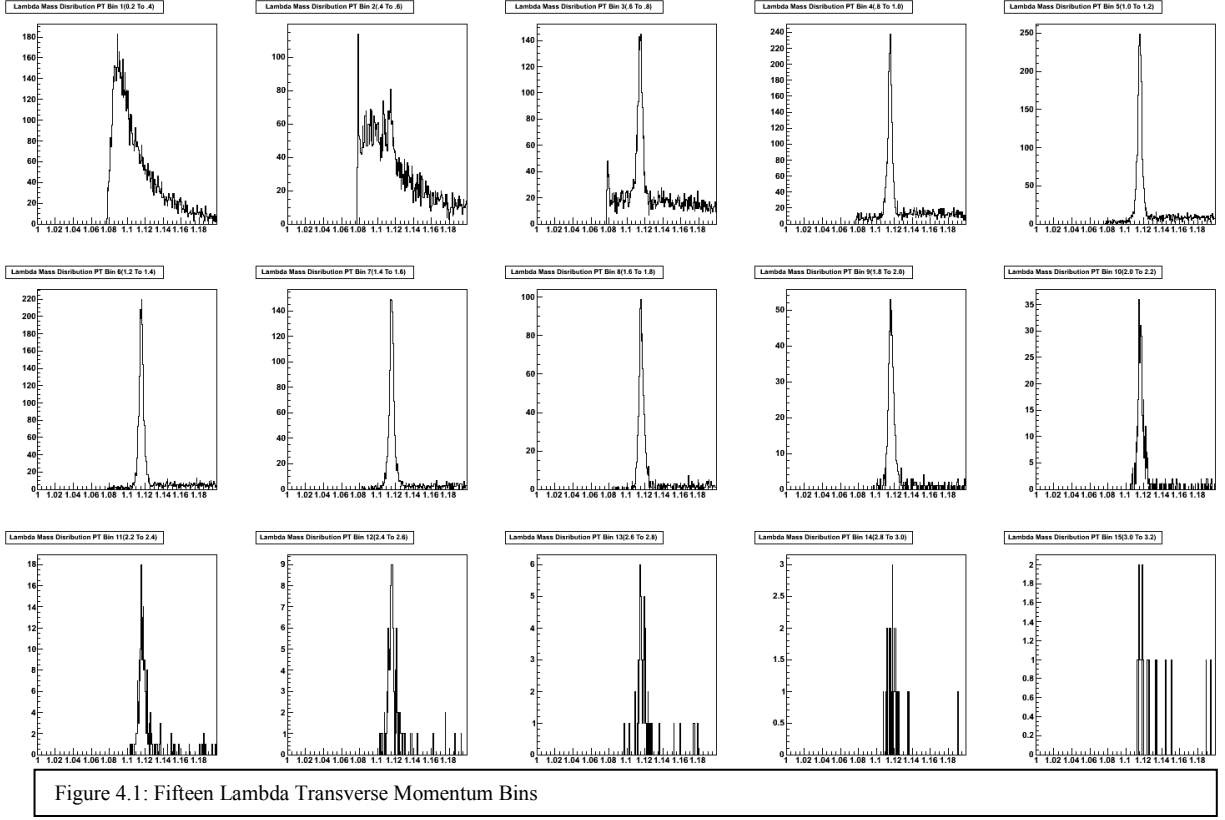
## Chapter 4: Transverse Momentum Spectrum

### 4.1 Transverse Momentum Binning

The next step in the analysis of the data was to form the mass peaks in different windows of transverse momentum. In the collision system, there are two components of momentum considered. There is a very large amount of momentum parallel to the beam line for each colliding nucleon. This is the direction in which the beam of gold nuclei was originally traveling through the two mile beam pipe. When the particles collide another component of momentum becomes relevant and it is referred to as transverse momentum. The term transverse comes from the fact that the momentum is perpendicular or transverse from the beam line. All transverse momentum is a result of the collision. If there was no collision, then the nuclei would continue traveling around the ring with their momentum parallel to the beam pipe axis. This provides a key insight into the nature of the material that was produced in the collision. By analyzing the spectrum of transverse momentum of various particles produced in the collision, aspects of the dynamics of the collision can be understood.

The procedure for building the mass peaks in transverse momentum bins is as follows. For each particle passing all cuts, the particles are broken down into their respective transverse momentum bins. For the final analysis, fifteen different bins of transverse momentum ranging from 0.2 to 3.2 GeV/c were used. Each bin has a width of 0.2 GeV/c. For the  $\Lambda$  particles there are significant peaks from the third transverse momentum bin until the twelfth bin. Transverse momentum bins thirteen through fifteen suffer from low statistics and these bins are not used for this analysis. There are relatively few high transverse momentum  $\Lambda$  particles to fill the higher bins as the transverse momentum spectrum falls off exponentially.





For each of the  $K_S^0$ ,  $\Lambda$ , and anti- $\Lambda$  particles the transverse momentum bins produced were in regions of 0.2 GeV/c. The binning went as follows:

Bin1: 0.2 – 0.4	Bin 6: 1.2 – 1.4	Bin 11: 2.2 – 2.4
Bin 2: 0.4 – 0.6	Bin 7: 1.4 – 1.6	Bin 12: 2.4 – 2.6
Bin 3: 0.6 – 0.8	Bin 8: 1.6 – 1.8	Bin 13: 2.6 – 2.8
Bin 4: 0.8 – 1.0	Bin 9: 1.8 – 2.0	Bin 14: 2.8 – 3.0
Bin 5: 1.0 – 1.2	Bin 10: 2.0 – 2.2	Bin 15: 3.0 – 3.2

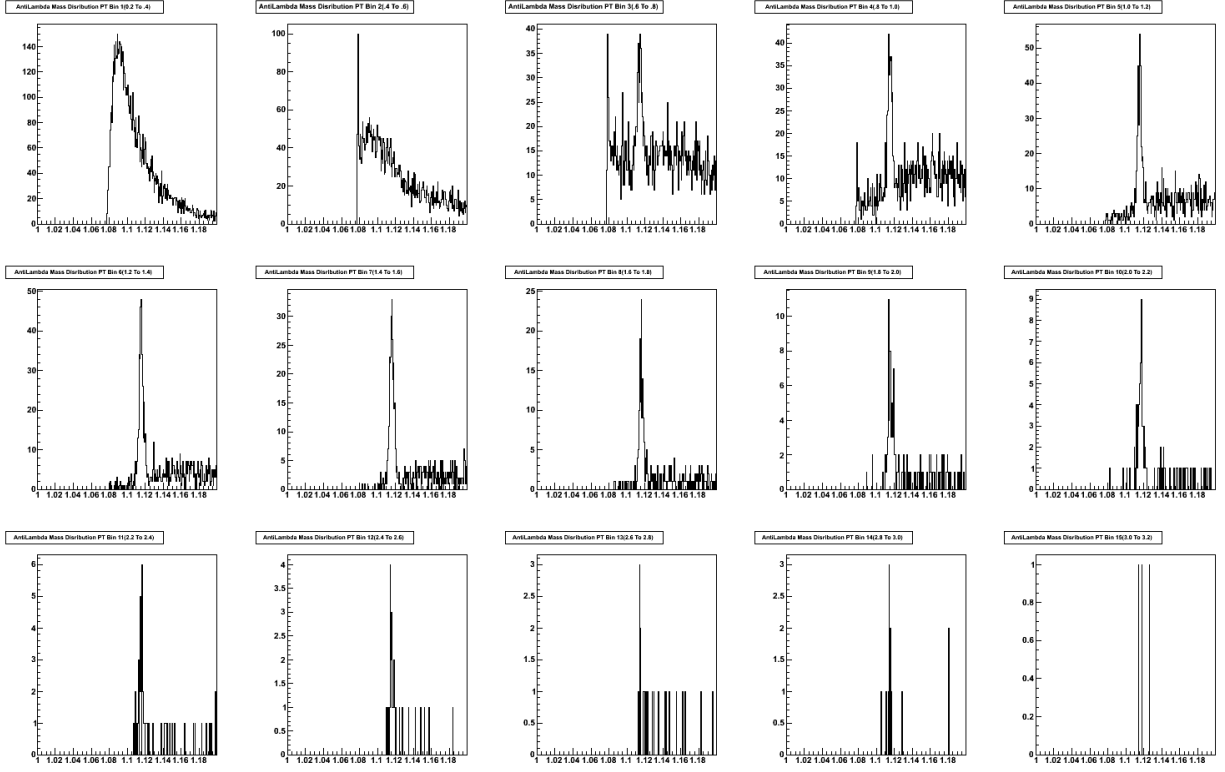


Figure 4.2: Fifteen Anti-Lambda Transverse Momentum Bins

The anti- $\Lambda$  transverse momentum bins show the high level of residual background from the cut tuning explained in the previous chapter. As expected, the higher bins of transverse momentum break down completely due to the lack of statistics. This was also seen in the  $\Lambda$  particles at high transverse momentum. Final corrections for the K0 shorts are still in production.

## 4.2 Transverse Momentum Spectrum

After the fifteen transverse momentum bins have been created for the  $K_S^0$ ,  $\Lambda$ , and anti- $\Lambda$  particles, the next step is to extract the yield, or total number of particles, in each bin to get a transverse momentum spectrum. To get the total number of  $K_S^0$ ,  $\Lambda$ , and anti- $\Lambda$  particles in each transverse momentum bin, the peaks have their sidebands subtracted in the same way as was done to get the minimum bias yield from the minimum bias mass distributions. Those numbers,

the total amount of  $K_S^0$ ,  $\Lambda$ , and anti- $\Lambda$  particles in each transverse momentum bin, are then plotted as shown in the following figures.

**Uncorrected Raw Lambda Transverse Momentum Spectrum**

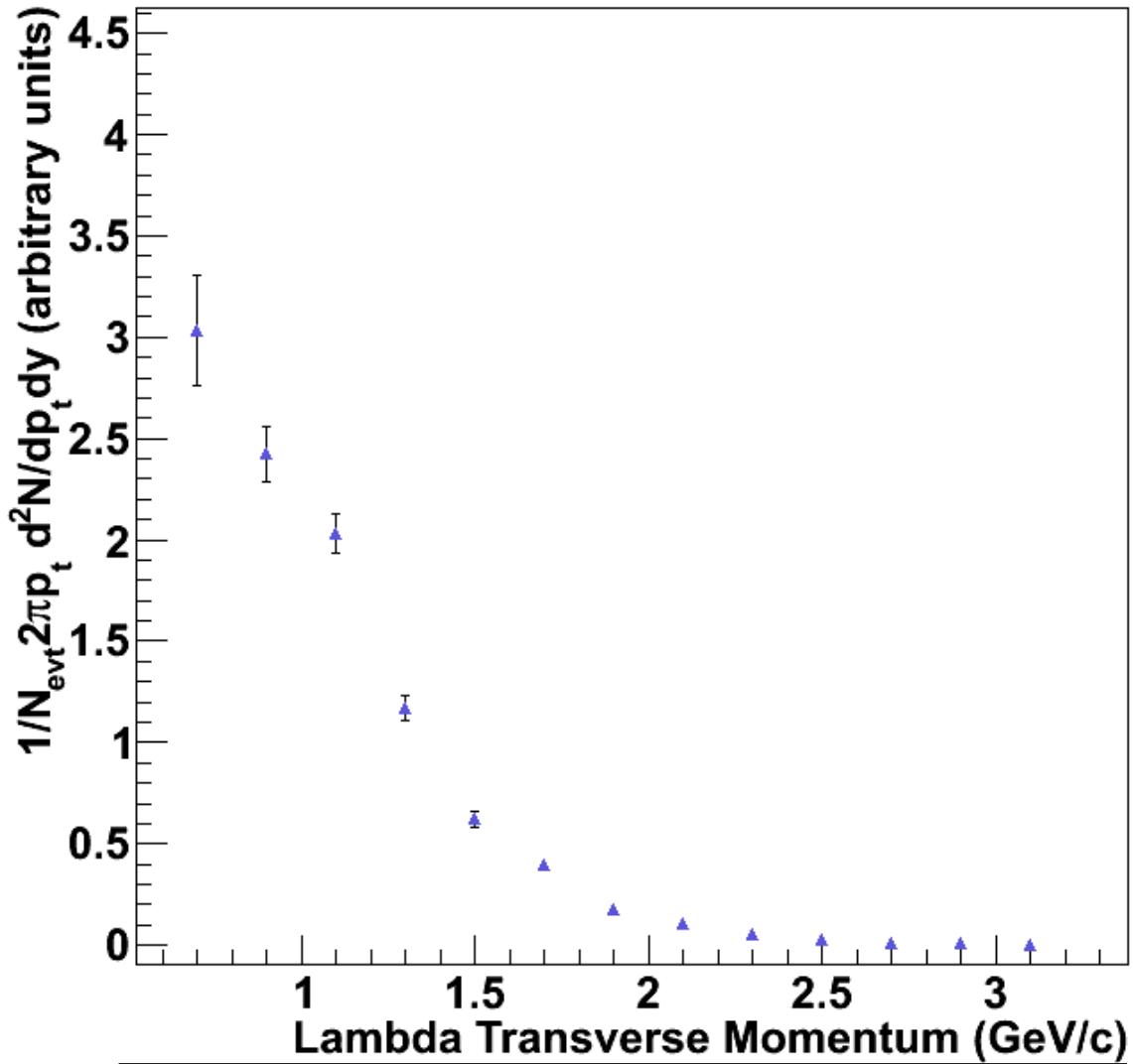


Figure 4.3: Lambda Transverse Momentum Spectrum

Bins above 2.5 GeV/c are not used due to the low statistics. This spectrum is exponential in nature and when the data is fitted in the next step the y-axis will be transformed into a log scale. The label on the y-axis stands for the invariant cross section. Each point on this plot is effectively the probability for production of the given particle at that value of momentum.

Uncorrected Raw AntiLambda Transverse Momentum Spectrum

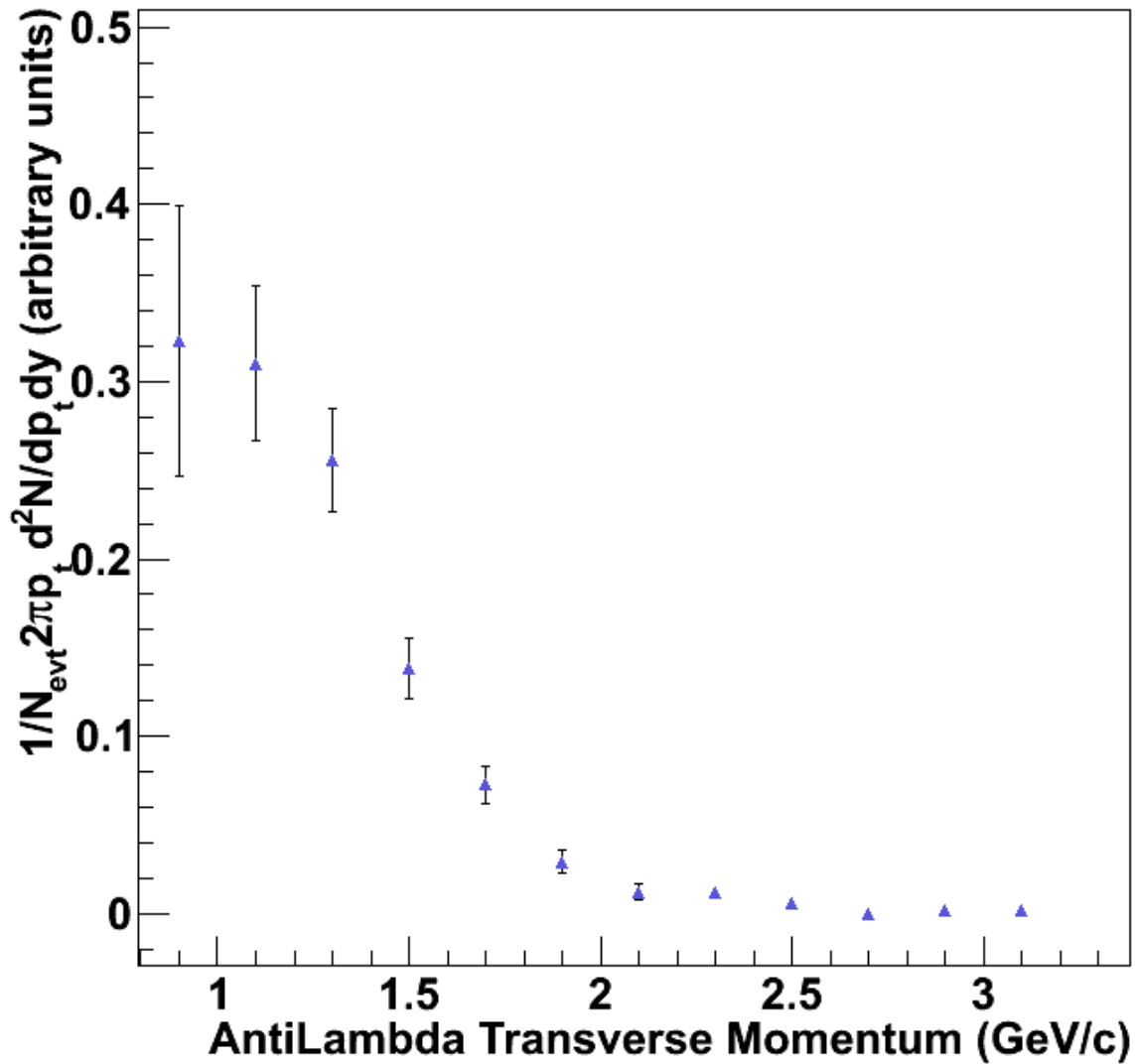


Figure 4.4: Anti-Lambda Transverse Momentum Spectrum

As expected the anti- $\Lambda$  spectrum seen above shows the larger errors bars in bins two through four due to the lower significance of the mass peaks displayed in figure 4.2. Again, the high transverse momentum bins are not used due to the low numbers of anti- $\Lambda$  particles.

In these graphs we see high levels of  $\Lambda$  and anti- $\Lambda$  particles produced at lower transverse momentum. This makes sense because many of the particles that come out of the collision zone

maintain a significant component of momentum parallel to the beam, therefore we see most of the particles created at low transverse momentum.

The next step in understand the transverse momentum spectrum is to fit the spectrum with an equation. The plots are fitted with a Boltzmann red curve, which is discussed in the next chapter. The fitted plots are shown below. The “ $\sqrt{s}$ ” stands for the center of mass of the collision, and for my research the center of mass was 19.6 GeV.

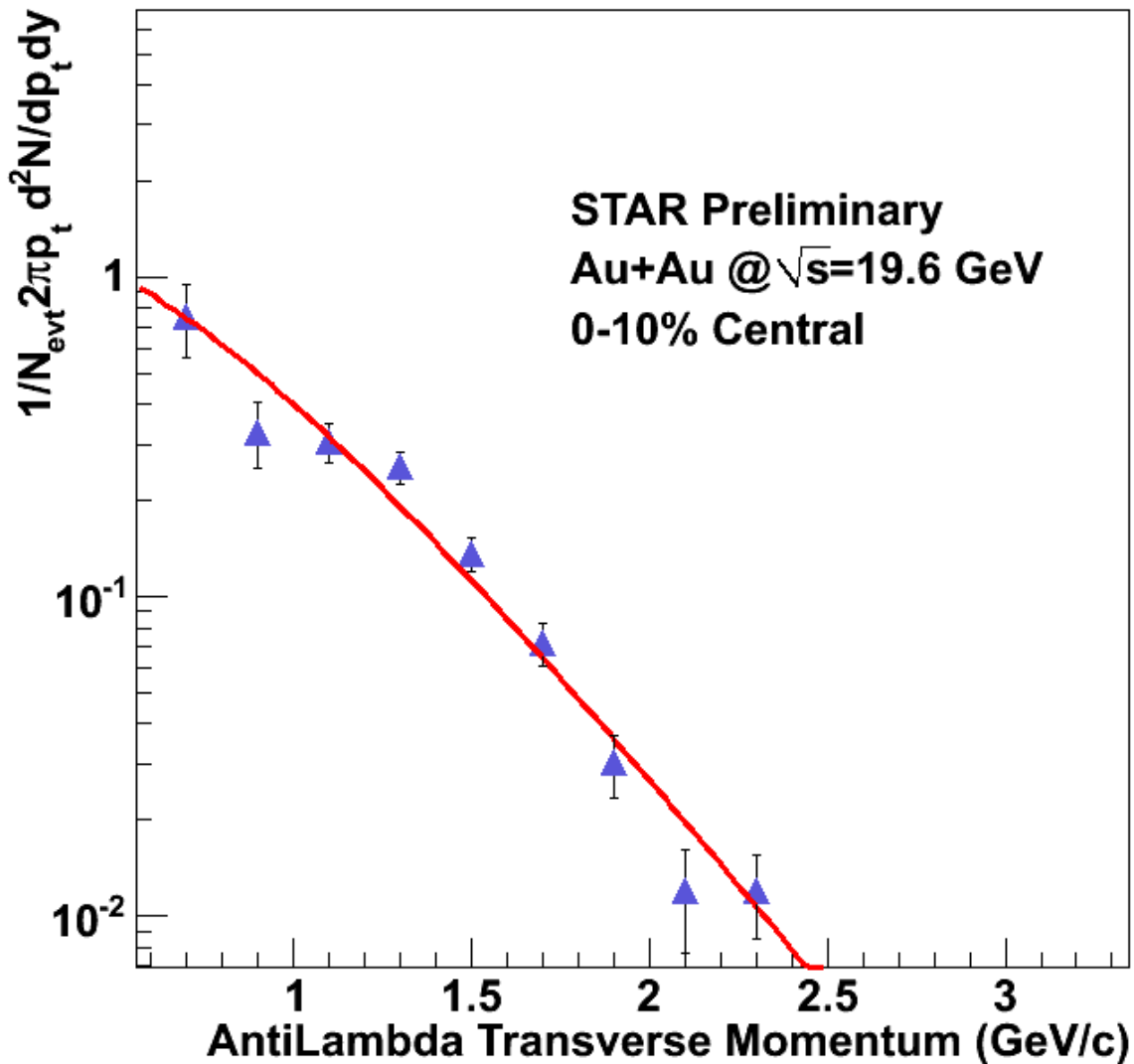


Figure 4.5: Lambda Transverse Momentum Spectrum with Fit

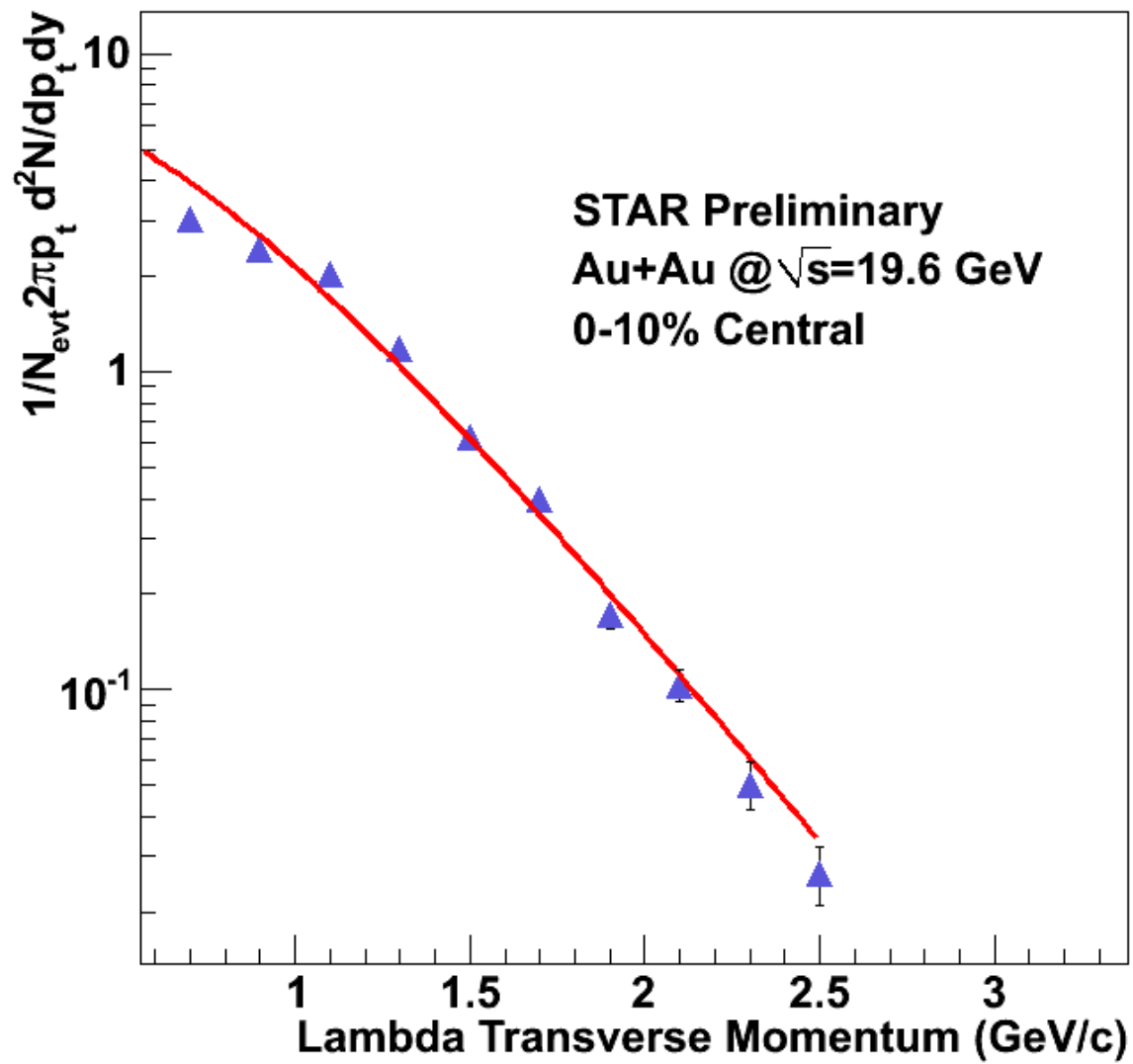


Figure 4.6: Anti-Lambda Transverse Momentum Spectrum with Fit

## Chapter 5: Corrections

Once the raw analysis is complete the next step is to apply corrections to the data. Corrections must be applied because not all of the  $K_S^0$ ,  $\Lambda$ , and anti- $\Lambda$ s that are produced in the collision actually are able to enter into the Time Projection Chamber. Some of the particles continue traveling down the beam pipe because they were originally travelling at nearly the speed of light. The software that is used to recreate the tracks is not perfect, and the signals we are tracking are real and therefore contain some degree of noise. Occasionally the software used to recreate the tracks makes mistakes and misses particles needed for the analysis. There is a high density of tracks in the time projection chamber and sometimes when the tracker is following a track it grabs another close by track and follows the new track. This is crossover tracking and is one of the errors with the tracking software. Another instance of is track splitting. During the data collection, sometimes one of the pad planes for detection is turned off. A track may start in one pad plane, cross through the pad plane that is turned off, and then enter another pad plane. The software occasionally recognizes that as one track, and sometimes it reconstructs two different tracks. Corrections are produced to account for these software issues and are then applied to the raw data to get a final result.

In order to have successfully corrected data, the events must be put through the embedding chain. The first step in this process is to look at the events at the signal level. We want to simulate the detectors response to the particles in which this project is examining. Each simulated lambda decays to two simulated daughters and the TPC simulator, GEANT, provides us with simulated detector level signals which can then be embedded into real data with the aim at testing our efficiency at reconstructing them for real events. For each raw event the event multiplicity, or number of particles, and the vertex position are inputted in the GENTX program,

a program that recreates simulated particles. Five percent of the total multiplicity of the event is added to the reconstructed event. In essence, if there is a one-hundred track collision, then five  $\Lambda$  particles are generated. The  $\Lambda$  particles are created with equal probability over the measured range of transverse momentum and rapidity. The  $\Lambda$ 's that are generated isotropically decay into protons and pions in the rest frame of the parent, or  $\Lambda$ , particle. The daughter particles, protons and pions, are then propagated throughout a simulator of the STAR TPC via the GEANT software. The program accounts for energy loss and ionization from the simulated  $\Lambda$  daughters that enter the TPC. In final step these detector level signals are embedded into the set of signals from the real event. This is where the process of embedding gets its name; the generated signals are literally embedded into the real events.

Once the new tracks have been embedded, the event is passed to the reconstruction chain. This set of generated and real signals are tracked and analyzed to see how many of the found tracks are associated with generated particles. By comparing this output with the real analysis determine the acceptance and efficiency corrections for the time projection chamber for the specific events produced. Because efficiency is not constant the embedding process needs to be run for every analysis and every centrality in each analysis. Below are plots of the efficiency and acceptance corrections for the Lambda particle in four different centrality classes.



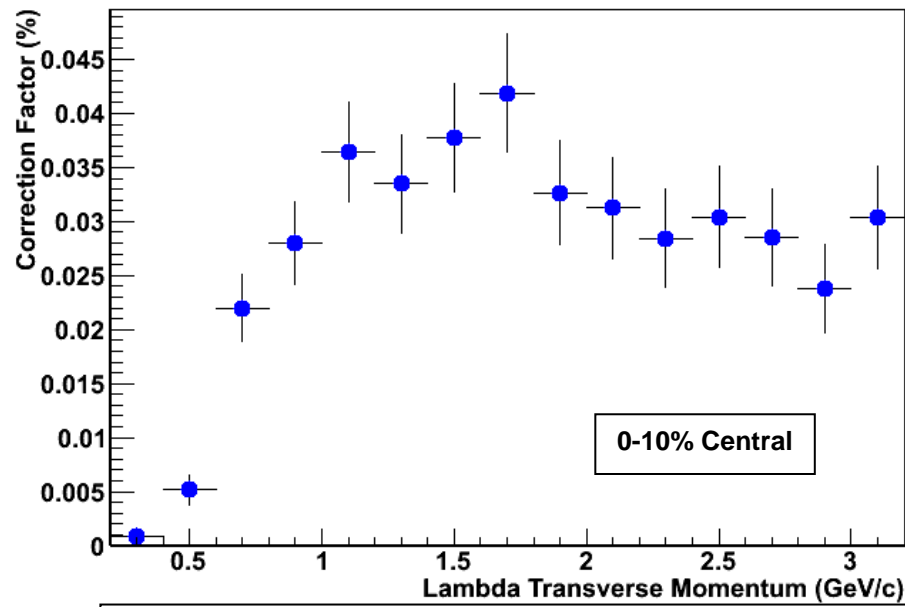


Figure 5.1: Plot of Correction Factor for Lambda Particles versus Transverse Momentum for 0-10% Central collisions.

RCLambdas

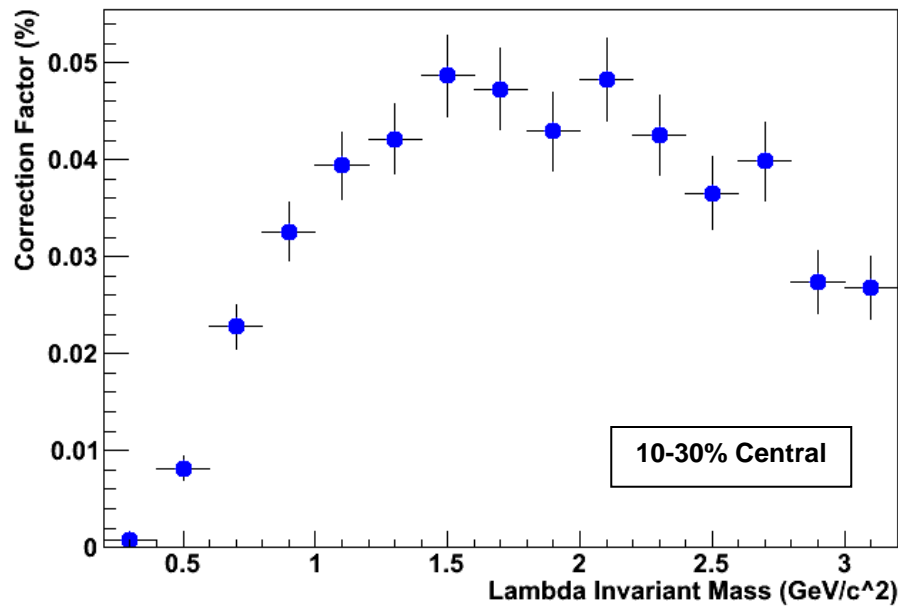


Figure 5.2: Plot of Correction Factor for Lambda Particles versus Transverse Momentum for 10-30% Central collisions.

RCLambdas

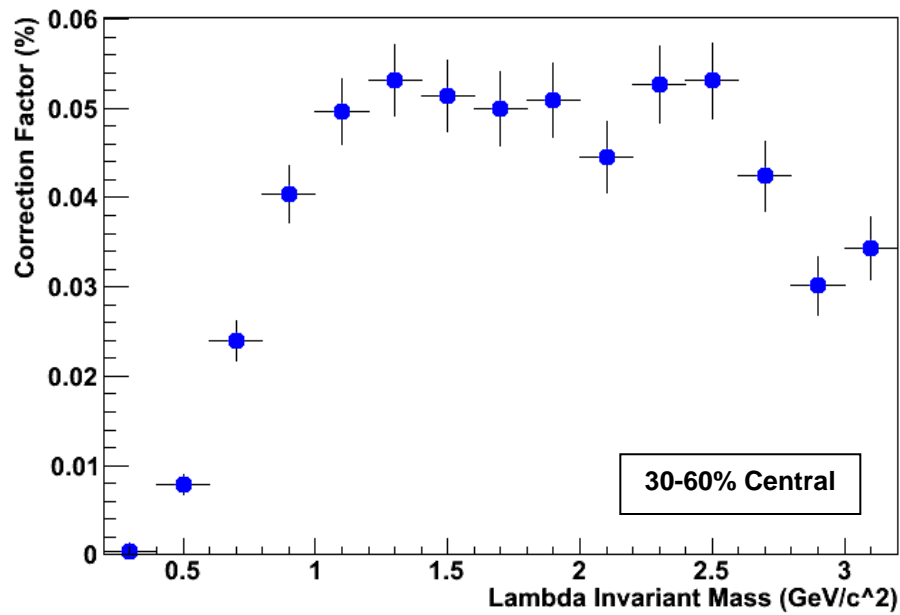


Figure 5.3: Plot of Correction Factor for Lambda Particles versus Transverse Momentum for 30-60% Central collisions.

RCLambdas

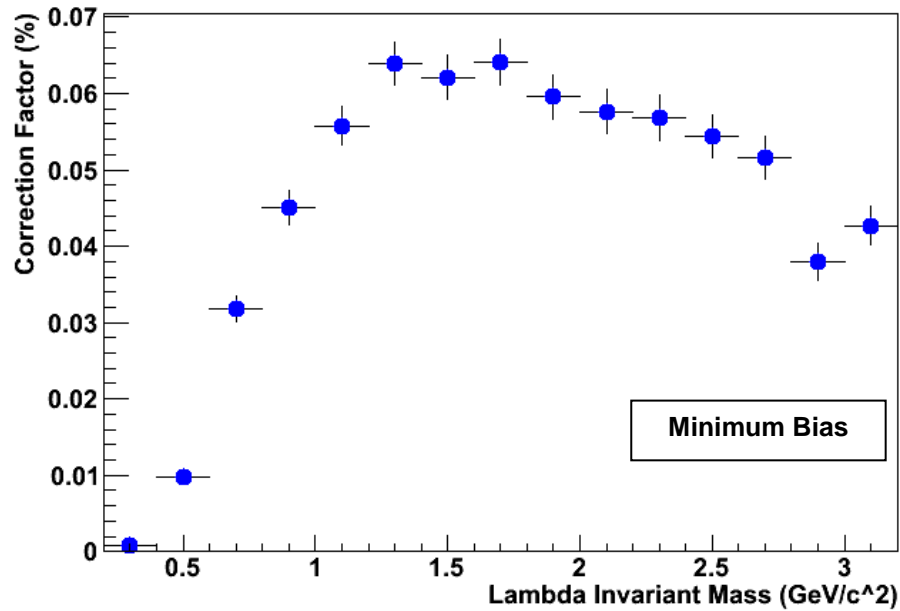


Figure 5.4: Plot of Correction Factor for Lambda Particles versus Transverse Momentum for Minimum Bias, all centralities examined.

In figure 5.4 the term “Minimum bias” is used. This simply means that all of the collisions were examined, there was no centrality discriminator. A check on the embedding results is to compare what different distributions from simulations look like relative to the same distributions from real data. Those plots are shown below.

**Decay Length of V0**

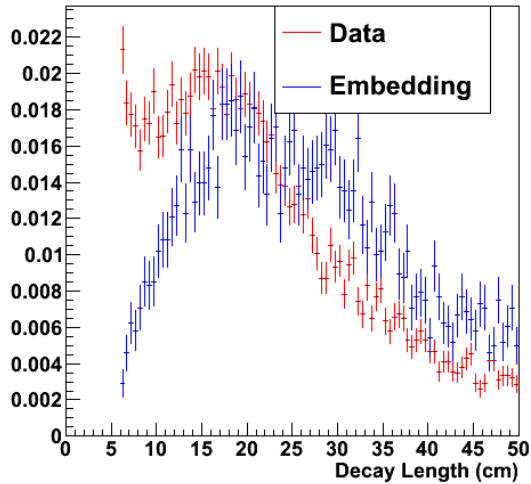


Figure 5.5: Decay Length of the V0 for both the embedded and real events.

**RCDcaDaughters**

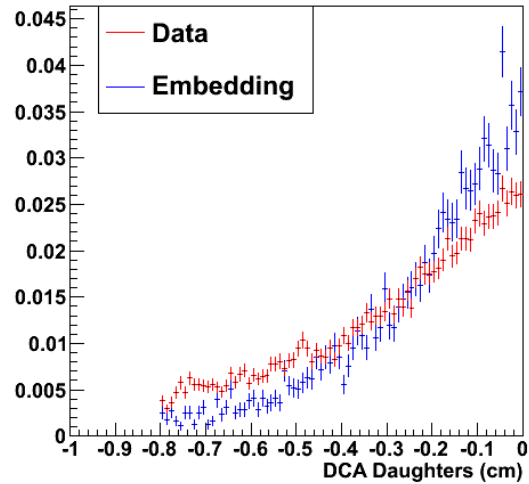


Figure 5.6: Distance of Closest Approach of the Daughters for both the embedded and real events.

**RCDcaNegToPV**

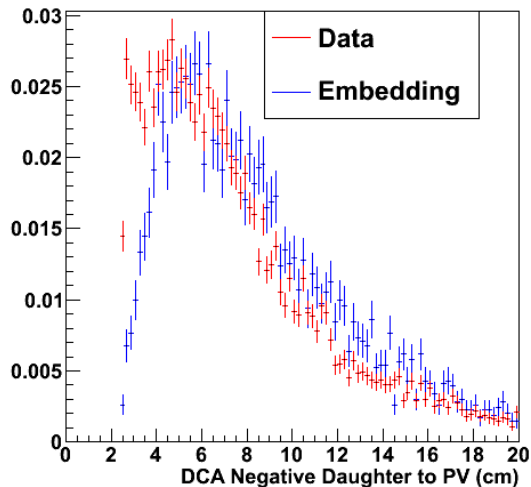


Figure 5.7: Distance of Closest Approach of the Negative Daughter to the Primary Vertex for both the embedded and real events.

**NHits on Negative Daughter**

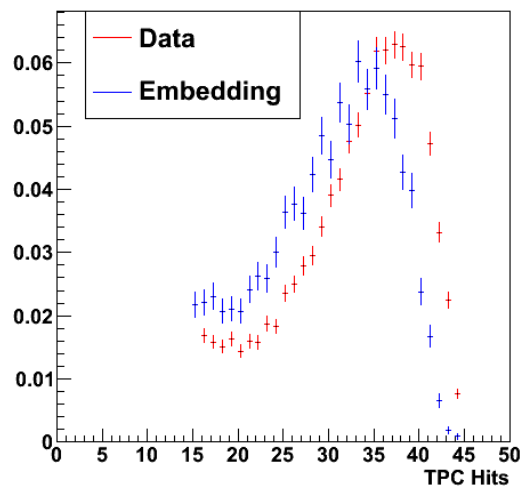


Figure 5.8: Number of Detector Hits of the Negative Daughter for real and embedded events

RCDcaPosToPV

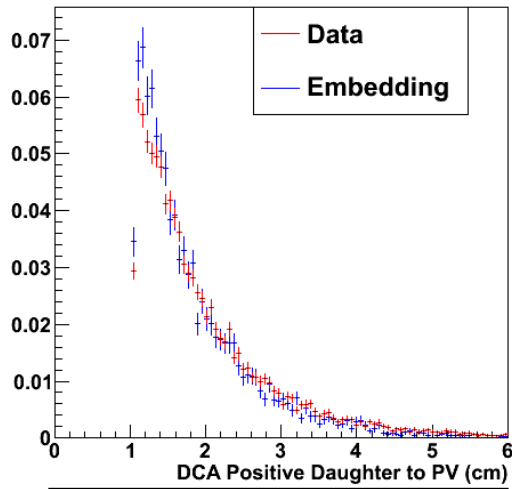


Figure 5.9: Distance of Closest Approach of the Positive Daughters to the Primary Vertex for both the real and embedded data.

NHits on Positive Daughter

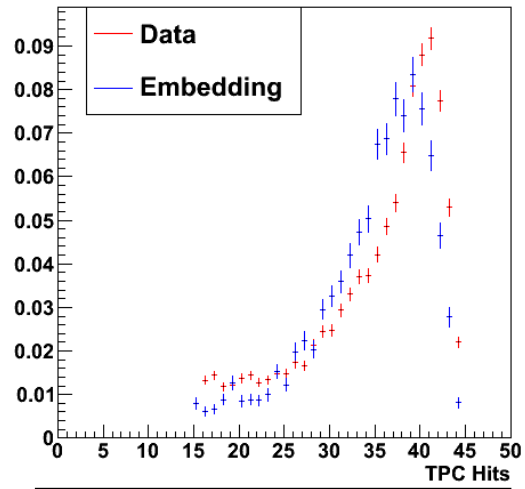


Figure 5.10: Number of Detector Hits of the Positive Daughter for real and embedded events

RCV0DcaToPV

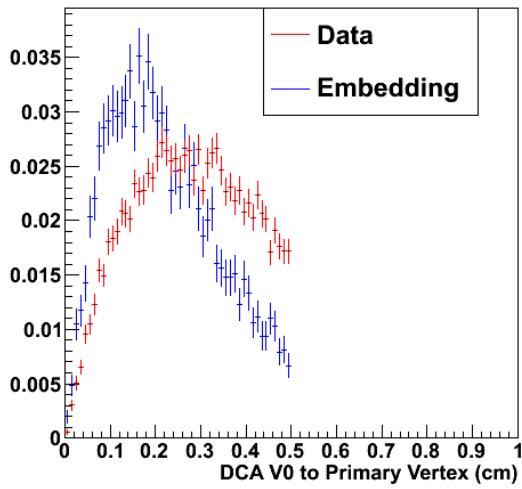


Figure 5.11: Distance of Closest Approach of the VO to the Primary Vertex for real and embedded events

In figure 5.5 and 5.7 there is a divergence at lower levels of decay length between the data and the embedding. The data is higher and primarily comes from background tracks at lower transverse momentum. These tracks are false daughters and are not real lambdas. As the decay length gets smaller and smaller, all tracks point back to the primary vertex and it is easier to

mistake a lambda for a non-lambda. In figure 5.11 there is a discrepancy that results from background that exists underneath the mass peak. The peak in this graph is broader for the real data than for the embedding and this is a result of the added background from the false lambdas.

## Chapter 6: Results

### Lambda Transverse Momentum Spectrum

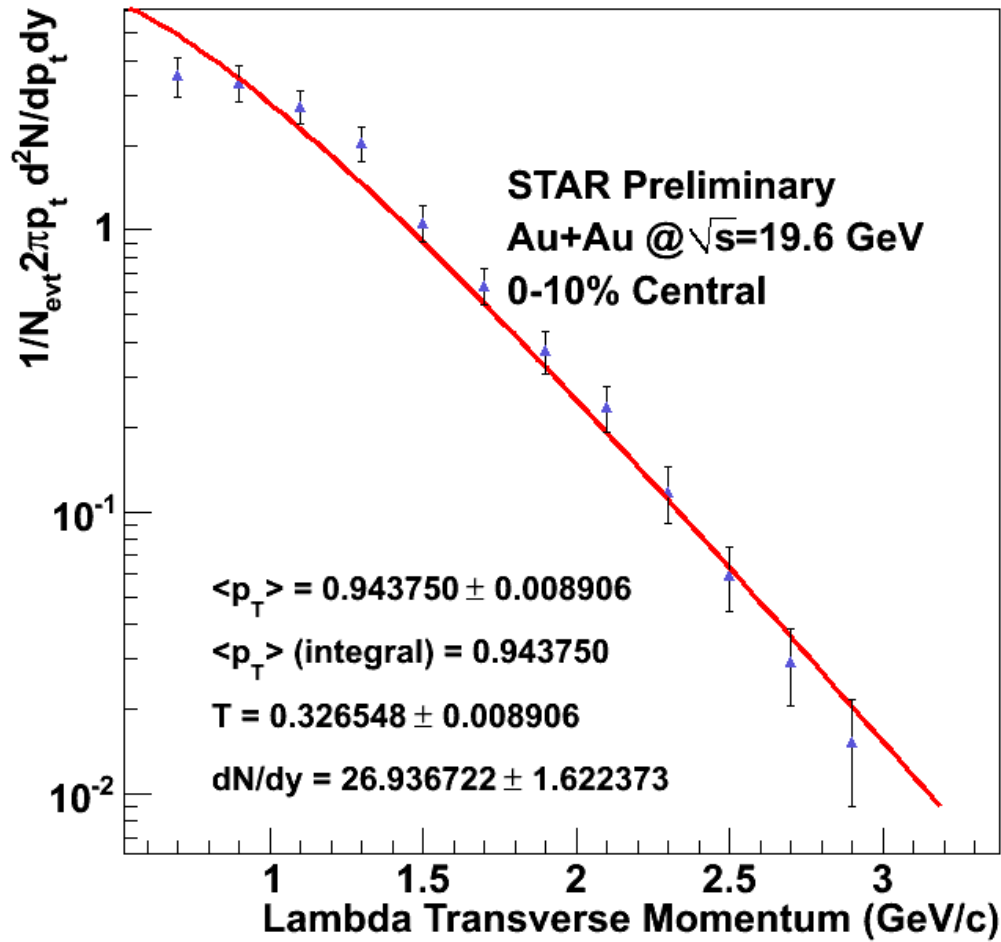


Figure 6.1: Corrected Lambda Transverse Momentum Spectrum with Boltzmann Fit.

The transverse momentum in figure 6.1 is the final corrected result for this project. It is shown on a semi-log scale so that the shape can be better seen. A few important quantities are shown in the figure. The particle yield, or  $dN/dy$ , is the number of particles per unit of rapidity per event. The average transverse momentum over the whole spectrum is 0.94 GeV/c within the quoted uncertainty, and is given by the symbol  $\langle p_T \rangle$ .  $T$ , or the inverse slope parameter is a

characterization of the steepness of the fall-off of the invariant cross section with respect to momentum.

The red curve represents the Boltzmann fit to this data. The equation programmed into the code that produced this curve is shown in the following equation.<sup>14</sup>

$$\frac{1}{2\pi m} \frac{\partial^2 N}{dy dm} = \frac{m dN/dy}{2\pi T(mo^2 + 2moT + 2T^2)} e^{-(m-mo)/T}$$

A Boltzmann function is used because it represents the thermal model for quark-gluon on plasma. The thermal model is used for a few important reasons. One, it assumes that a fireball, whether it is QGP or a hadronic gas, exists and is in a state of local equilibrium. The thermal model claims that there is chemical equilibrium and thermal equilibrium. Thermal equilibrium is reached through inelastic and elastic scattering processes and allows a temperature to be defined for the system. Chemical potentials exist in systems where chemical equilibrium has not been established, in the thermal model, there are no chemical potentials. This equilibrium defines the particle yields and ratios.<sup>15</sup> The thermal model is used because it provides a simple basis for which a theoretical description of these collisions.

Another result is the Anti-Lambda to Lambda ratio, shown in figure 6.2. This is an important data point that is used to compare against the results that were measured by different experiments around the globe, such as at SPS (Super Proton Synchrotron), and AGS (Alternating Gradient Synchrotron). The ratio rests at 0.18 with an uncertainty of 0.8 for this data. This ratio gives insight into the nature of the collision. In a baryon-rich scenario, or a collision where many

---

<sup>14</sup> Matthew A.C. Lamont, "Neutral Strange Particle Production in Ultra-Relativistic Heavy Ion Collisions at 130 GeV." *Thesis for PhD*. University of Birmingham, January 2002, pg 109.

<sup>15</sup> Ibid, 40.

baryons exists, there would be a suppression of anti-baryons, because few were being created. This would lead to a higher number of Lambdas and a lower ratio. In a baryon-free scenario, there is going to be equal amounts of anti-baryons and baryons produced. This would mean that the ratio should be closer to unity. Our measurement of 0.18 would seem to indicate that at lower energies, the collision region is not baryon free and some mixed state of hadron gas and QGP may be a better approximation than pure QGP.

### AntiLambda to Lambda Ratio Plot

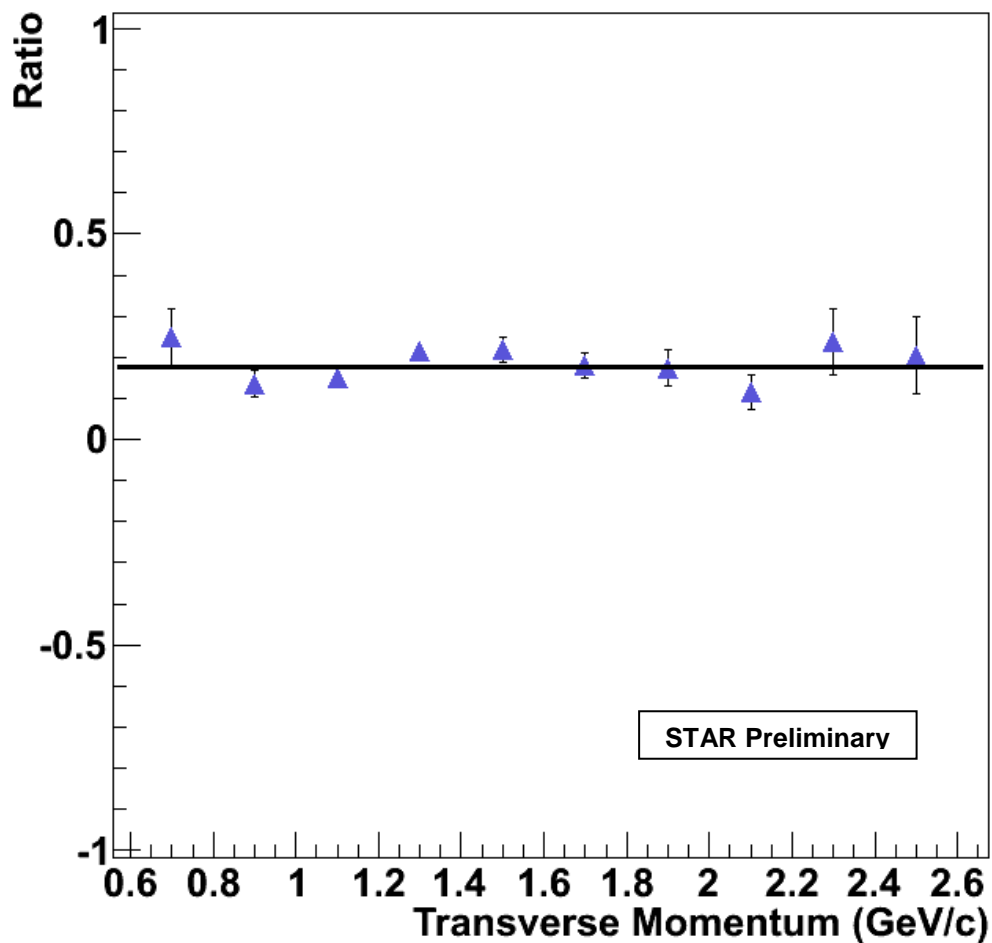


Figure 6.2: Anti-Lambda to Lambda Ratio versus Transverse Momentum



Also, the measurement is flat across the measured range of transverse momentum. This observation indicates that the same mechanism is responsible for Lambda or Anti-Lambda production over the full range of transverse momentum. A difference in production mechanism would introduce a step or possibly even a step in this observable.

## Chapter 7: Conclusions and Outlook

The goal of this project was to produce results that can be compared with similar analyses that have been done by experiments at other particle accelerators and to resolve the NA57:NA49 discrepancy. This discrepancy is a 20 percent difference in their respective studies of anti-baryon/baryon measurements, and in the mid-rapidity Lambda yield itself. The following shows the world's data on Lambda production from three machines, the Alternating Gradient Synchrotron (AGS), the Super Proton Synchrotron (SPS), and RHIC. AGS is the lowest energy, ranging from 1 GeV to 9 GeV. SPS is in the middle and the ranges shown here vary from 9 GeV to about 20 GeV. The figure below shows the particle yield compared to data from SPS and AGS. The result from this project is higher than originally anticipated and is in better agreement with the NA57 result than that from NA49.

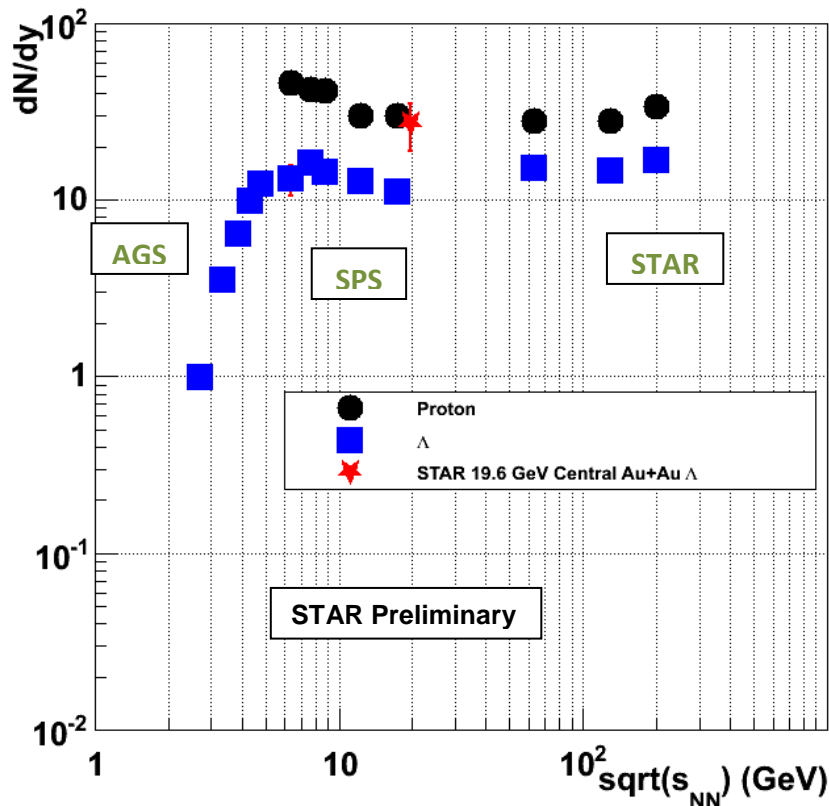
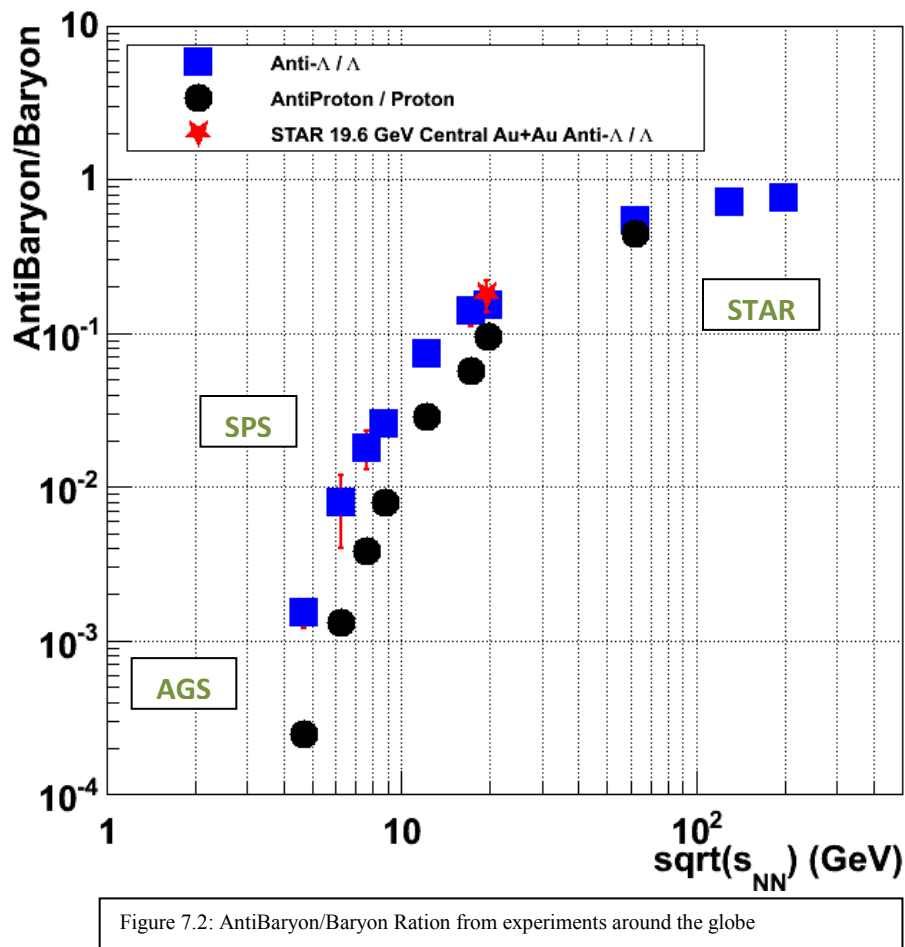


Figure 7.1:  $dN/dy$ , or Particle Yield, compared to data from the rest of the world.

Next we compare the measured Anti-Lambda to Lambda ratio with other experiments. The figure below shows that the data that was produced from this result coincides with the results produced at SPS and AGS in terms of the Anti-Baryon/Baryon ratio. The high energy STAR points are shown on the right, and the point produced from this analysis is represented by the red star.



Another deliverable for this project was to resolve the discrepancy between NA57 and NA49 between their Anti-Lambda to Lambda measurements at around 20 GeV. From this project, it can be stated that STAR data is closer to the result produced in NA57, rather than NA49.

Research is a continuum and discovering further physical truths does not stop with the conclusion of this project. The next steps in the continuation of this project would be to examine why the  $dN/dy$  yield is slightly higher than anticipated, by about one standard deviation.

Different models, other than the thermal models, could be compared to this transverse momentum spectrum. Nevertheless this project represents a successful contribution to the field of heavy ion physics and the results will go to a journal of the American Physical Society.

## **Acknowledgements**

This report could not have been written without the guiding wisdom of my advisor and friend, Dr. Richard Witt. Over the course of three years he has taught me everything I know about this subject and even more about life in general. I cannot thank him enough. Secondly, this project would never have occurred without the support and love of my fiancée, Dominique Fleury Bastine. Her ever present patience, understanding, and love allowed me to successfully learn and achieve. I also would like to thank the STAR Collaboration and the Trident Committee for funding and supporting this project.